Research Square

Preprints are preliminary reports that have not undergone peer review.
They should not be considered conclusive, used to inform clinical practice,
or referenced by the media as validated information.

Human RIG-I Antiviral Deficiency Caused by a Dominant-Negative Variant Trapped in a Signaling-Inactive State

Smita Patel

patelss@rutgers.edu

Rutgers University https://orcid.org/0000-0002-2523-4933

Mihai Solotchi

Rutgers Medical School

Huie Jing

National Institute of Allergy and Infectious Diseases

Emma Gebauer

National Institute of Allergy and Infectious Diseases https://orcid.org/0009-0003-5138-9685

Scott Novick

The Herbert Wertheim UF Scripps Institute for Biomedical Innovation & Technology

Bruce Pascal

Omics Informatics

Wesley Tung

National Institute of Allergy and Infectious Diseases, National Institutes of Health
https://orcid.org/0000-0002-4577-3926

Pranita Hanpude

Rutgers University

Luigi Apollon

Rutgers University

Talia Madura

Rutgers University

Yu Zhang

National Institute of Allergy and Infectious Diseases

Camille Alba

Uniformed Services University of the Health Sciences https://orcid.org/0000-0002-0458-1629

Basak Kayaoglu

National Institute of Allergy and Infectious Diseases, National Institutes of Health

Annalisa Saracino

Azienda Ospedaliero-Universitaria Consorziale Policlinico di Bari

Paola Laghetti
University of Bari Aldo Moro
Anna Volpe
University of Bari
Imad Isehak
National Institute of Allergy and Infectious Diseases, National Institutes of Health
Elana Shaw
National Institute of Allergy and Infectious Diseases, National Institutes of Health
Lindsey Rosen
National Institutes of Health
Colin Sweeney
National Institute of Allergy and Infectious Diseases, National Institutes of Health
https://orcid.org/0000-0002-9442-1134
Steven Holland
Laboratory of Clinical Immunology and Microbiology, Division of Intramural Research, National Institute of Allergy and Infectious Diseases, National Institutes of Health https://orcid.org/0000-0003-3207-5464
Andrea Lisco
National Institute of Allergy and Infectious Diseases https://orcid.org/0000-0002-1475-356X
Clifton Dalgard
Department of Anatomy, Physiology & Genetics, Uniformed Services University of the Health Sciences
https://orcid.org/0000-0003-2025-8239
Joseph Marcotrigiano
National Institute of Allergy and Infectious Diseases https://orcid.org/0000-0001-7670-7836
Patrick Griffin
The Herbert Wertheim UF Scripps Institute for Biomedical Innovation & Technology
https://orcid.org/0000-0002-3404-690X
Helen Su
NIAID, NIH https://orcid.org/0000-0002-5582-9110

Article

Keywords:

Posted Date: August 20th, 2026

DOI: https://doi.org/10.21203/rs.3.rs-10667618/v1

License: This work is licensed under a Creative Commons Attribution 4.0 International License.
Read Full License

Additional Declarations: There is **NO** Competing Interest.

Human RIG-I Antiviral Deficiency Caused by a Dominant-Negative Variant Trapped in a Signaling-Inactive State

Mihai Solotchi [1,2,#], Huie Jing [3,4,#], Emma Gebauer [5], Scott J Novick [6], Bruce D Pascal [6,7], Wesley Tung [3,4,8], Pranita Hanpude [1], Luigi Apollon [1,2], Talia Madura [9], Yu Zhang [3,4], Camille Alba [10,11], Basak Kayaoglu [3,4], Annalisa Saracino [12], Paola Laghetti [13], Anna Volpe[14], Imad A Isehak [3,4], Elana R Shaw [3,4], Lindsey B Rosen [15], Colin L Sweeney [16], Steven M Holland [15], Andrea Lisco [17], Clifton L Dalgard [10,18], Joseph Marcotrigiano [5*], Patrick R Griffin [6*], Helen C Su [3,4*], Smita S Patel [1,19*]

[1] Department of Biochemistry and Molecular Biology, Robert Wood Johnson Medical School, Rutgers University, Piscataway, NJ 08854, USA.

[2] Graduate School of Biomedical Sciences at the Robert Wood Johnson Medical School of Rutgers University, Piscataway, NJ 08854, USA.

[3] Human Immunological Diseases Section, Laboratory of Clinical Immunology and Microbiology, Division of Intramural Research, National Institute of Allergy and Infectious Diseases, National Institutes of Health, Bethesda, MD, 20892, USA.

[4] NIAID Clinical Genomics Program, Division of Intramural Research, National Institute of Allergy and Infectious Diseases, National Institutes of Health, Bethesda, MD 20892, USA.

[5] Structural Virology Section, Laboratory of Infectious Diseases, Division of Intramural Research, National Institute of Allergy and Infectious Diseases, National Institutes of Health, Bethesda, MD 20892, USA.

[6] Department of Molecular Medicine, The Wertheim UF Scripps Institute, Jupiter, FL 33458 USA.

[7] Omics Informatics, Honolulu, HI 96813, USA.

[8] NIH Oxford-Cambridge Scholars Program, Bethesda, MD 20892, USA.

[9] School of Environmental and Biological Sciences, Rutgers University, New Brunswick, NJ 08901, USA

[10] The American Genome Center, Center for Military Precision Health, Bethesda, MD 20814, USA.

[11] Henry Jackson Foundations for the Advancement of Military Medicine, Bethesda, MD 20817, USA.

[12] Clinic of Infectious Diseases, Department of Precision and Regenerative Medicine and Ionian Area (DIMEPRE-J), University of Bari Aldo Moro, Bari, Italy.

[13] Section of Pharmacology, Department of Precision and Regenerative Medicine and Ionian Area, School of Medicine, University of Bari Aldo Moro, Bari, Italy.

[14] Infectious Diseases Clinic, University of Bari, Bari, Italy.

[15] Immunopathogenesis Section, Laboratory of Clinical Immunology and Microbiology, Division of Intramural Research, National Institute of Allergy and Infectious Diseases, Bethesda, MD 20892, USA.

[16] Genetic Immunotherapy Section, Laboratory of Clinical Immunology and Microbiology, Division of Intramural Research, National Institute of Allergy and Infectious Diseases, National Institutes of Health, Bethesda, MD, 20892, USA.

[17] Mucosal and Cutaneous Viral Immunopathogenesis Unit, Laboratory of Immunoregulation, Division of Intramural Research, National Institute of Allergy and Infectious Diseases, Bethesda, MD 20892, USA.

[18] Department of Anatomy, Physiology & Genetics, Uniformed Services University of the Health Sciences, Bethesda, MD 20814, USA.

[19] Lead contact: patelss@rwjms.rutgers.edu

[#] Contributed equally

* Corresponding authors

ABSTRACT

RIG-I is a cytosolic pattern-recognition receptor that detects viral RNA to initiate type I interferon responses. While gain-of-function helicase mutations cause human autoinflammatory disease, naturally occurring loss-of-function variants in conserved helicase motifs remain undescribed. Here, we identify a heterozygous G731R substitution in helicase motif VI in a patient with life-threatening COVID-19 pneumonia. Patient-derived immune cells exhibit severe defects in RIG-I-dependent antiviral signaling. Mechanistically, G731R is an intrinsic dominant-negative loss-of-function variant that retains high-affinity binding to viral RNA and ATP but lacks RNA-stimulated ATPase activity. Hydrogen-deuterium exchange mass spectrometry and stopped-flow kinetic analyses reveal that G731R fails to undergo the conformational transitions required for productive CARD exposure, trapping RIG-I in an RNA-bound, signaling-inactive CTD-mode intermediate that competitively inhibits wild-type RIG-I. In contrast, distinct substitutions at the same residue bidirectionally tune receptor activity, with bulky charged residues producing loss-of-function phenotypes and small hydrophobic residues producing gain-of-function phenotypes. Studies of this first naturally occurring dominant-negative RIG-I variant demonstrate that the conserved helicase motifs function as ATP-dependent conformational checkpoints that couple viral RNA recognition to productive antiviral signaling.

INTRODUCTION

Viral infections pose a constant threat to human health, requiring rapid innate immune responses to limit viral replication and disease. Central to this defense are the RIG-I-like receptors (RLRs), a family of cytosolic pattern-recognition receptors comprising RIG-I, MDA5 (IFIH1), and LGP2 (DHX58), which detect viral RNAs and initiate type I interferon (IFN) responses [1-6]. Among these, RIG-I serves as a frontline sensor by recognizing viral RNAs containing 5′-triphosphate (5′ppp) or 5′-diphosphate (5′pp) double-stranded termini [7-10].

RIG-I is a multidomain SF2 helicase[11] comprising a central helicase core, tandem N-terminal caspase activation and recruitment domains (CARDs) that mediate downstream MAVS signaling, and a C-terminal domain (CTD) that specifically recognizes 5′ppp RNA termini (Figure 1A) [12-14]. In the absence of RNA, the CARDs are sequestered through intramolecular interactions with the Hel2i subdomain and the intrinsically disordered CARD-helicase linker (CHL), maintaining an autoinhibited state (Figure 1B-C PDB: 4A2W) [14-16].

RIG-I activation begins when the CTD recognizes the 5′ppp RNA terminus, forming a transient CTD-mode complex, which transitions to a stable helicase-mode, in which the helicase core encircles the double-stranded RNA stem, exposing the CARDs and CHL (Figure 1C) [9,14,17,18]. This transition is driven by closure of the Hel1-Hel2 interface, where ATP is coordinated by the conserved SF2 helicase motifs (motifs I-VI). The transition-state analog ADP·AlF_3-bound RIG-I captures a closed conformation, in which the Hel1 and Hel2 domains are in their closest position (Figure 1B, PDB: 4A36). Subsequently, ATP hydrolysis drives RIG-I translocation along the RNA duplex away from the 5′ppp RNA terminus, ultimately promoting RNA dissociation [17]. The ATP-dependent conformational transitions provide a proofreading mechanism that rapidly clears RIG-I from self-RNAs while permitting sustained engagement of viral RNAs at the 5’ppp RNA end to support antiviral signaling.

Naturally occurring human variants in helicase motifs provide a unique opportunity to decipher the structural roles of helicase motifs in RIG-I activation and their physiological consequences in human disease. Mutations in helicase motifs I (C268F) and II (E373A)

have been identified in patients with the autoinflammatory Singleton-Merten syndrome (SMS)[19,20]. Biochemically, these mutations impair ATP hydrolysis, allowing them to form long-lived complexes on RNA and to be activated by self-RNAs [17,21]. However, impaired ATP hydrolysis itself does not hyperactivate RIG-I. The engineered motif I mutant (K270A) binds RNA and is ATPase-deficient, yet is signaling-inactive via an unknown mechanism [1,17]. This indicates that helicase motifs play a key role in regulating RIG-I activation, although the mechanisms remain unknown.

While prevailing models suggest that viral RNA binding, or the coupled binding of RNA and ATP, is sufficient to activate signaling, it remains unclear whether ligand binding alone guarantees productive receptor conversion. Although ATP binding and hydrolysis provide a proofreading mechanism, the precise functional and regulatory roles of helicase motifs I-VI in driving RIG-I activation remain incompletely understood. Furthermore, no naturally occurring human loss-of-function mutations affecting these conserved helicase motifs have been described, leaving the physiological consequences and structural checks governing motif-dependent loss of function in human disease unknown.

As part of an ongoing genetic study of patients with severe respiratory viral infections, including severe COVID-19, we identified multiple rare deleterious RIG-I variants, including a previously unreported heterozygous G731R substitution within helicase motif VI (Figure 1A). G731 resides within the highly conserved RGR sequence of motif VI (Figure 1D-E), where the flanking arginine residues function as catalytic arginine fingers that coordinate ATP and its hydrolysis. Unlike the constitutively active ATPase-deficient Singleton-Merten syndrome variants, G731R is a loss-of-function mutant with an unusual dominant-negative phenotype. This provides a unique opportunity to study RIG-I deficiency, define its molecular basis, and understand how helicase motif VI regulates the ATP-dependent conformational transitions that couple viral RNA recognition to receptor activation.

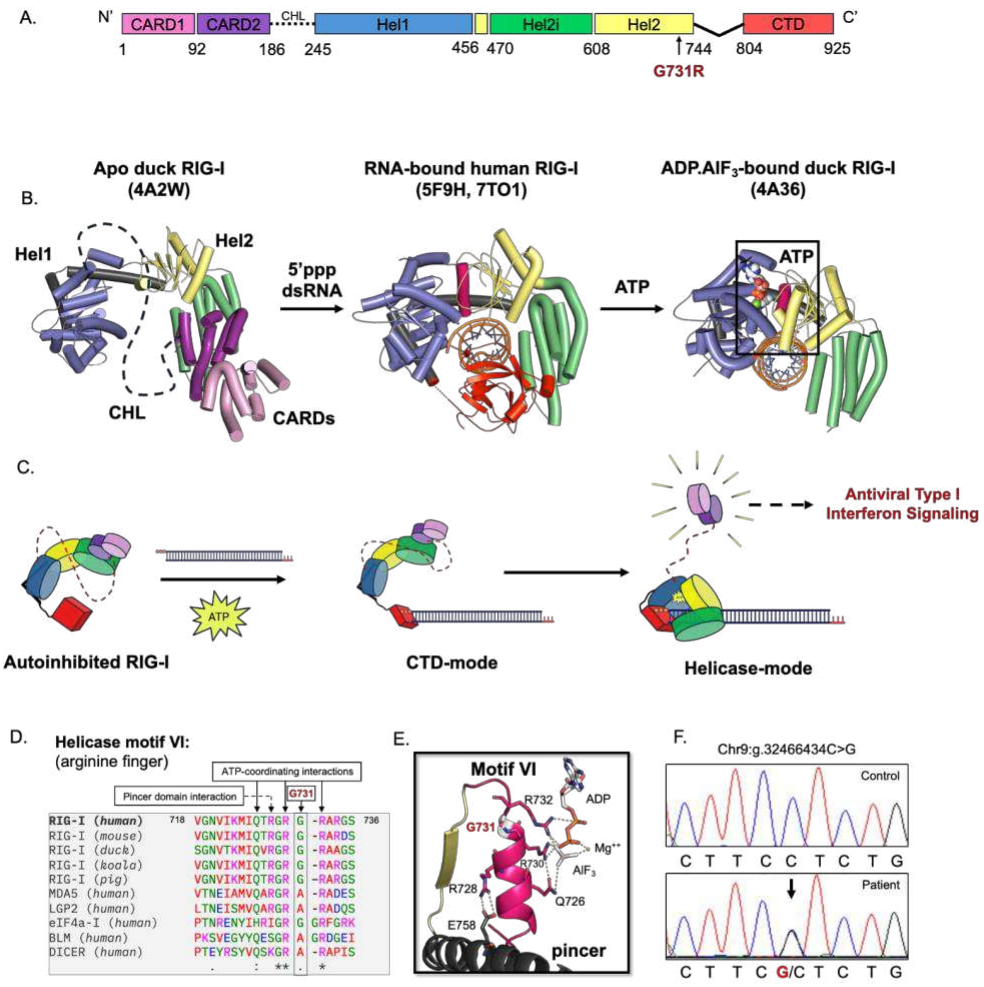


Figure 1. Novel RIG-I G731R mutation identified in a severe COVID-19 patient.
(A) Domain structure of human RIG-I. The arrow indicates the G731 location.
(B) RNA- and ATP-induced conformational activation of RIG-I. Top view of apo duck RIG-I (PDB: 4A2W) with CARDs (pink/purple) sequestered to Hel2i domain (green) autoinhibitory interface and helicase domains in an open conformation, semi-closed RNA-bound human RIG-I (PDB: 5F9H), and closed RNA-bound duck RIG-I with ADP·AlF_3 (PDB: 4A36).
(C) Cartoons show the RNA-binding pathway of RIG-I proposed from previous studies[17].
(D) Clustal Omega Multiple Sequence Alignment[53] of helicase motif VI in RIG-I of various species, RLRs, and other SF2 RNA helicases.
(D) Zoomed-in view of motif VI (in pink) in the closed state of RIG-I (PDB: 4A36).
(E) Chromatograms from Sanger sequencing of genomic DNA showing a heterozygous C to G mutation in the patient, indicated by the arrow.

Here, we define the mechanistic basis of G731R dysfunction using integrated cellular, biochemical, biophysical, and hydrogen-deuterium exchange mass spectrometry (HDX-MS) analyses. We show that G731R retains high-affinity viral RNA and ATP binding, but fails to undergo the ATP-dependent conformational transition that converts it into a signaling-competent closed helicase complex. Consequently, G731R becomes trapped in a signaling-inactive intermediate that competitively inhibits wild-type RIG-I, explaining its dominant-negative phenotype. Remarkably, distinct substitutions at

G731 produce either loss- or gain-of-function phenotypes, identifying G731 and helicase motif VI as a finely tuned regulator of RIG-I activation. Together, these findings identify the first naturally occurring dominant-negative RIG-I variant and establish the conserved helicase motifs as ATP-dependent conformational checkpoints that determine whether recognition of viral RNA culminates in productive antiviral signaling.

RESULTS

Identification of RIG-I G731R variant in a patient with life-threatening COVID-19

Since numerous studies using mouse models and tissue culture systems support a role for RIG-I in antiviral immunity [22-25], we hypothesized that pathogenic variants associated with impaired RIG-I function might be present in patients with severe viral infections. In our longstanding search among patients referred to us for increased susceptibility to various respiratory viruses, including SARS-CoV-2 and influenza virus, we identified multiple rare deleterious RIG-I variants. Here, we focus on one previously unreported heterozygous variant, G731R, with a unique dominant-negative phenotype, providing an opportunity to investigate the mechanism of RIG-I activation. This patient, a 63-year old Caucasian male with no preexisting comorbidities or prior history of severe viral infections, was hospitalized with critical COVID-19 pneumonia requiring invasive mechanical ventilation (patient information and clinical presentation in Methods). Whole genome sequencing revealed a heterozygous *RIGI* variant (chr9:g.32466434C>G, NM_014314.4:c.2191G>C, NP_055129.2, p.Gly731Arg), which was confirmed by Sanger dideoxy sequencing (Figure 1E). No variants were detected in other genes known to regulate the type I IFN pathway (Table S1). This *RIGI* variant has not been previously reported in the Genome Aggregation Database (gnomAD) population database and was computationally predicted to be deleterious (CADD score 29.7 and AlphaMissense score 0.9725).

Patient-derived immune cells carrying G731R show severe defects in RIG-I signaling

To determine whether the G731R variant impairs endogenous RIG-I function, we examined immune cells obtained from the patient. cDNA sequencing demonstrated comparable expression of the WT and G731R alleles in both T cells and monocyte-derived dendritic cells (MoDCs) (Figure 2A). Similarly, RIG-I protein levels in the patient's T cells were comparable to those of healthy donor controls at baseline and following IFN-α stimulation (Figure 2B). As RIG-I is itself an IFN-stimulated gene (ISG), its normal upregulation indicated that responses downstream of type I IFN receptors are unimpaired.

Despite normal RIG-I expression, stimulation with the RIG-I agonists 5′ppp ds39 RNA (Table S5) or 5′ppp hairpin RNA elicited little or no induction of IFN-β in the patient's T cells or MoDCs compared with healthy donor controls (Figure 2C-F). These findings demonstrate that the heterozygous G731R mutation severely compromises endogenous RIG-I-dependent type I IFN responses in primary human immune cells.

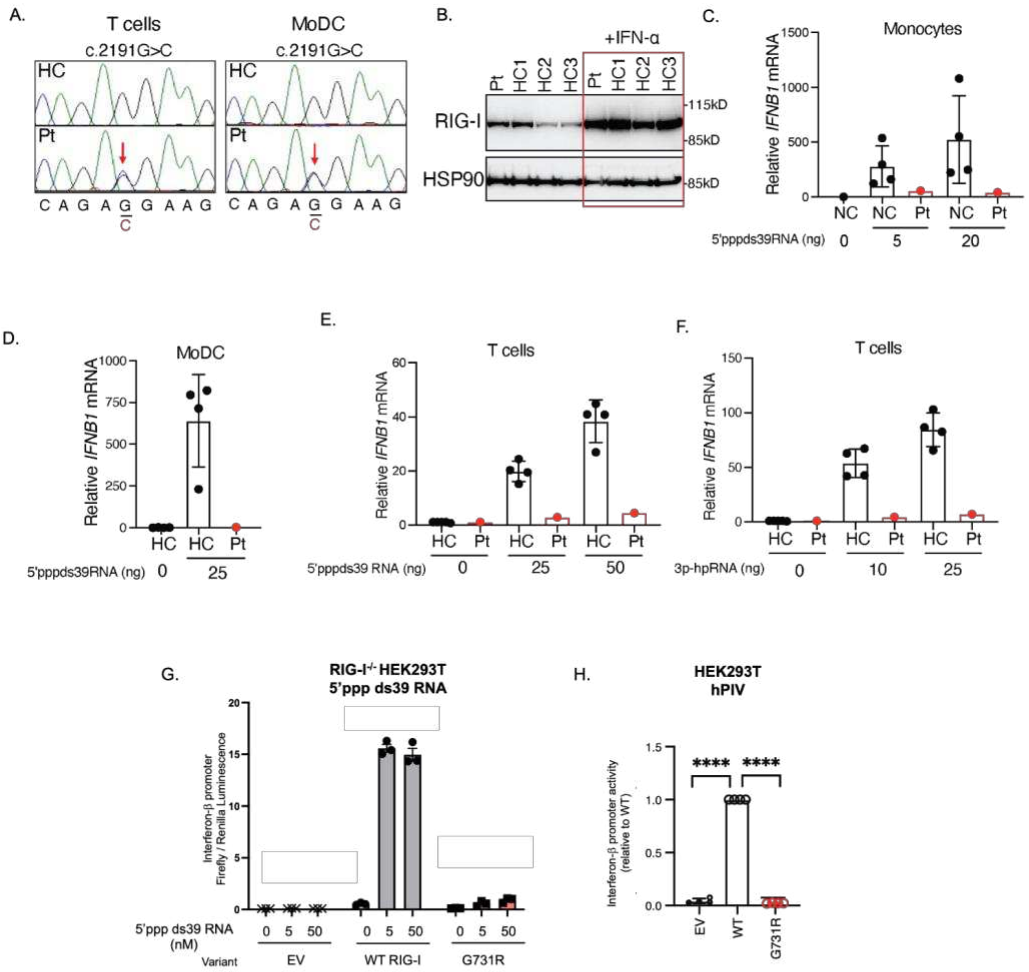


Figure 2. Impaired type I IFN responses in the patient cells upon stimulation with RIG-I specific ligands.
(A) Sanger dideoxy sequencing chromatograms of cDNA from the patient's T cells and monocyte-derived dendritic cells (MoDCs) showing a heterozygous G-to-C transversion corresponding to G731R, indicated by the arrows. HC: healthy control; Pt: patient.
(B) Immunoblot analysis of RIG-I proteins in whole cell lysates (90 μg/lane) from healthy controls (HC, n=4) and patient's cycling T cells, without or with IFN-α stimulation. HSP90 was used as a loading control.
(C-F) Primary monocytes (C), MoDCs (D), or T cells (E, F) from the patient were stimulated for 3 h with the indicated amounts per million cells of intracellular 5'ppp39dsRNA (C, D, and E) or 3p-hpRNA (F). *IFNB1* expression was quantified by qRT-PCR, normalized to that of *ACTB*, and shown relative to the average of normal controls. Data are mean ± SD from different individuals in each group. Data for unstimulated cells shown in panels (E) and (F) were shared in simultaneously run experiments.
(G) IFN-β promoter response from transfection of RIG-I plasmids (50 ng) into HEK293T RIG-I$^{-/-}$ cells measured by dual luciferase reporter assay (independent RNA transfections, n=3).
(H) hPIV-induced IFNβ reporter luciferase activities for G731R. HEK293T cells were transfected with WT, G731R, or EV along with the IFNβ-Luc and a constitutively expressed Renilla reporter for 6 hours. Cells were then infected with hPIV (MOI 3) for an additional 20 hours before measuring luciferase activity. IFNβ-Luc reporter activity in each condition was normalized to Renilla and then presented relative to WT RIG-I. Data show means ± SD from 3 independent experiments. Statistical analysis was performed using one-sample t-test. ****, P<0.0001.

G731R is an intrinsic loss-of-function RIG-I variant

To determine whether the signaling defect is intrinsic to the mutant protein, we next examined G731R in a reconstituted RIG-I signaling system using RIG-I$^{-/-}$ HEK293T cells

expressing either WT RIG-I or G731R under the control of the constitutive CMV promoter (Figure 2G). RIG-I-dependent activation of the IFN-β promoter was quantified using a dual-luciferase reporter assay. In the absence of ligand, WT RIG-I produced low basal IFN-β promoter activity that was robustly stimulated by the RIG-I substrate 5′ppp ds39 RNA (Table S5). In contrast, G731R showed minimal activation of the IFN-β promoter even at saturating RNA concentrations, consisting with an intrinsic loss of signaling activity.

Because RIG-I is essential for antiviral responses to paramyxoviruses, we next challenged cells with human parainfluenza virus (hPIV). Whereas WT RIG-I robustly activated the IFN-β reporter following infection, G731R failed to stimulate signaling (Figure 2H). Western blots confirmed that WT and G731R proteins were expressed at comparable levels (Figure S1A-C), indicating that the signaling defect was not due to reduced protein expression. Together, these results establish G731R as an intrinsically defective loss-of-function RIG-I variant.

G731R is a dominant-negative loss-of-function RIG-I variant

Because the patient carried a heterozygous G731R mutation, we next investigated whether the mutant protein exerts a dominant-negative effect on WT RIG-I. To examine this under physiological conditions, we sequentially transduced RIG-I-knockout human primary fibroblasts with lentiviruses expressing WT RIG-I followed by either G731R or empty vector (EV), generating WT+G731R and WT+EV cells, respectively (Figure 3A, S2A-B). Reconstitution with WT RIG-I markedly suppressed hPIV3 replication compared with RIG-I-knockout cells (Figure 3B-C, S2C). However, G731R alone failed to restrict viral replication, confirming that G731R is a loss-of-function variant. More importantly, hPIV3 replication was significantly higher in WT+G731R cells than in WT+EV cells (Figure 3D-E, S2D-J), demonstrating that G731R compromises the antiviral activity of WT RIG-I in a dominant-negative manner.

To quantify this effect in a reconstituted signaling system, WT RIG-I was co-expressed with increasing amounts of G731R in RIG-I$^{-/-}$ HEK293T cells. G731R inhibited 5′ppp ds39 RNA-induced IFN-β reporter activity in a dose-dependent manner (Figure 3F, S1B). Interestingly, G731R did not inhibit the basal response of WT RIG-I

(Figure S1D). G731R also suppressed hPIV-induced IFN-β reporter activity in a dose-dependent manner (Figure 3G). To model the patient's heterozygous genotype, equal amounts of WT RIG-I were co-transfected with either WT RIG-I (WT/WT) or G731R (WT/G731R). Compared with the WT/WT condition, WT/G731R exhibited markedly reduced IFN-β reporter activity (Figure 3H, S1G). Together, these findings demonstrate that G731R is a dominant-negative loss-of-function variant that suppresses the antiviral activity of WT RIG-I.

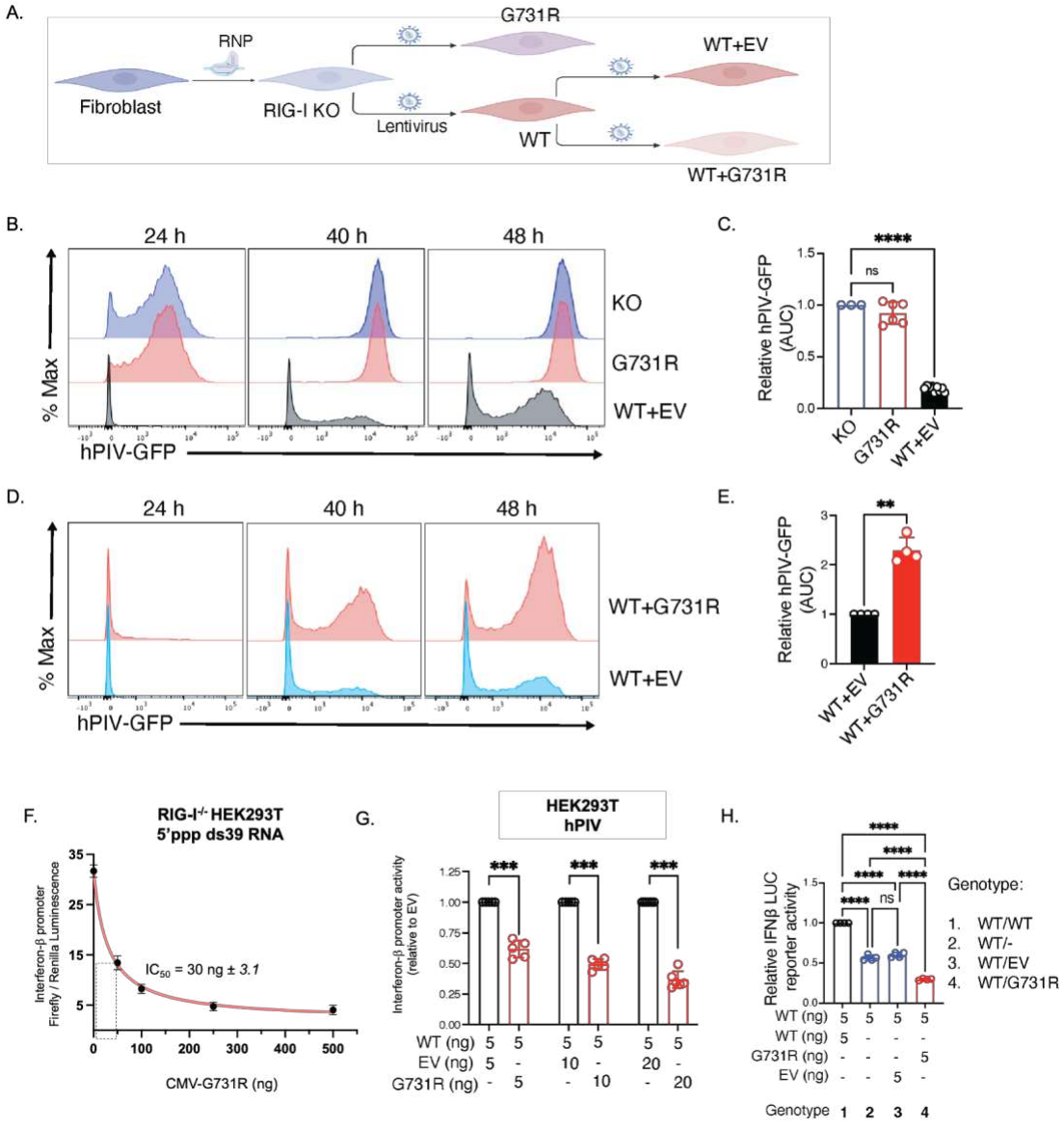


Figure 3. RIG-I G731R is a loss-of-function variant with a dominant negative phenotype.
(A) Experimental workflow for generating fibroblasts co-expressing WT and G731R RIG-I. Human primary fibroblasts were transfected with Cas9 protein/RIG-I gRNA (RNP) to knock out (KO) RIG-I. KO fibroblasts were then transduced sequentially with lentiviruses expressing WT RIG-I followed by either G731R or empty vector (EV). As an additional control, RIG-I KO cells were also transduced with lentivirus expressing G731R alone. See also Figure S2.
(B) Human primary RIG-I KO fibroblasts, either alone or transduced with RIG-I G731R or WT plus EV (WT+EV), were infected with GFP-expressing hPIV (MOI 0.2) for 24 to 48 h. Representative flow cytometry plots of hPIV-infected cells.
(C) hPIV infection was quantified by the area under the curve (AUC) of GFP MFI and shown relative to that of KO cells in each experiment from 3 independent experiments. In each experiment, 2 cell lines for G731R and 3 cell lines for WT+EV transduced cells were used.
(D) Human primary RIG-I KO fibroblasts transduced with WT RIG-I, plus either G731R RIG-I (WT+G731R) or EV (WT+EV), were infected with hPIV (MOI 0.2) for 24 to 48 h. hPIV infection was quantified by GFP expression. Shown are flow cytometry plots for a representative experiment.
(E) GFP was quantified by AUC of GFP MFI and shown relative to that of WT+EV cells in each experiment (N=4) (E). Data for WT+EV shown in panels (**C**) and (**E**) were shared in simultaneously run experiments. Statistical analyses were performed using one-sample t-test (F, H). ****, $P < 0.0001$; **, $P < 0.01$.
(F) IFN-β promoter response measured by dual luciferase reporter assay in HEK293T RIG-I$^{-/-}$ cells transfected with a constant amount of WT RIG-I plasmid and 5 nM 5'ppp ds39 RNA, while titrating G731R plasmid. Total plasmid concentration was kept constant by substitution with an empty vector. The error bars represent the standard error of the mean (independent RNA transfection, n=3), and the curve shows the fit of the mean data to equation 1 to obtain the half-maximal inhibitory concentration (IC_{50}).
(G) hPIV-induced IFNβ reporter luciferase activities in cells co-transfected with WT (5 ng) and increasing doses (5 to 20 ng) of G731R or EV plasmids. IFNβ-Luc reporter activity in each condition was first normalized to Renilla and then shown relative to EV. Data show means ± SD from 3 independent experiments. Statistical analysis was performed using one-sample t-test. ***, $P<0.001$
(H) Cells were co-transfected with WT RIG-I (5 ng) and an equal amount (5 ng) of WT RIG-I, G731R RIG-I, or empty vector (EV) plasmids to mimic the indicated genotypes, and then infected with hPIV. IFNβ-driven Firefly luciferase reporter activity for each condition was normalized to *Renilla* luciferase and shown relative to that of the WT/WT condition. RLU, relative light units. Data show means ± SD from 3 independent experiments. Statistical analysis was performed using one-way Anova with Turkey's multiple comparisons test. ****, $P < 0.0001$

G731R binds to 5'ppp dsRNA with a high affinity

As this patient was among the first reported to exhibit near-complete RIG-I functional deficiency, we sought to understand the biochemical mechanism underlying the loss-of-function and the dominant-negative effect of the G731R mutation. We first assessed whether the mutant could engage with 5'ppp dsRNA. Electrophoretic Mobility Shift Assay (EMSA) showed that G731R RIG-I binds to 5'ppp ds39 RNA with and without ATP to a similar extent as WT RIG-I (Figure 4A). RIG-I has a footprint of 10 bp on the RNA; hence, 5'ppp ds39 RNA supports WT RIG-I monomers and dimers that transition to form higher oligomers with RIG-I translocation in the presence of ATP (Figure 4A)[16,17]. Interestingly, G731R binds primarily as a monomer and forms fewer multimers on the 5'ppp ds39 RNA.

To quantify the binding affinity of G731R for the 5′ppp RNA, we used a fluorescence polarization-based titration assay (Figure S3A). G731R showed high affinity binding to fluorescein-labeled 5′ppp 10-bp hairpin (HP) RNA (Table S5), with a K_D value of 0.8 nM compared to 1.2 nM for WT RIG-I (Figure S3B). However, the fluorescence polarization

amplitude of the G731R complex was lower than that of WT (Figure S3C), indicating conformational differences between the RNA-bound states of WT and G731R.

To confirm that G731R also binds to 5'ppp ds39 RNA, which was used in the cellular assays, we used a competition assay to measure the binding affinity. The WT or G731R complex with fluorescein 5'ppp 10-bp HP RNA was challenged with increasing concentrations of unlabeled 5′ppp ds39 RNA (Figure S3D). In both cases, 5'ppp ds39 RNA displaced the HP RNA, indicating that 5'ppp ds39 binds to G731R. From the IC_{50} values (Figure S3E), we estimated the K_i or the K_D value of 3 nM for WT RIG-I and 1.2 nM for G731R (Figure 4B and Figure S3F). Thus, G731R binds 5′ppp ds39 RNA with ~3-fold higher affinity than WT RIG-I (Figure 4B, P = 0.0151).

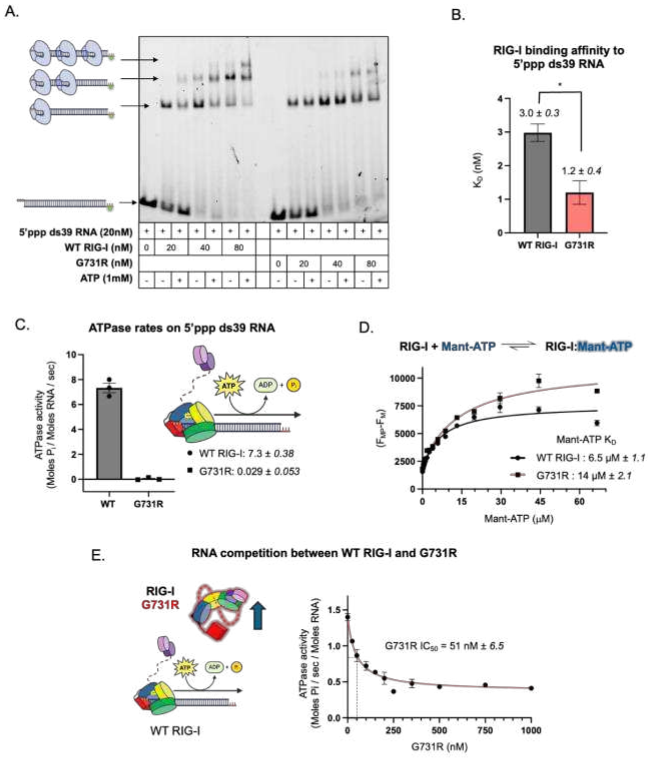


Figure 4. RIG-I G731R competitively binds 5'ppp dsRNA in an ATPase deficient manner.
(A) Electrophoretic mobility shift assay of fluorescently labeled 5'ppp ds39 RNA upon addition of WT and G731R RIG-I (representative image from n=3).
(B) 5'ppp ds39 RNA binding affinity (K_D) was obtained using a competitive fluorescence-based RNA binding assay. See Figure S3. First, 5'ppp 10bp HP RNA (FAM) binding affinity (K_D) was measured by changes in fluorescence polarization while titrating RIG-I against constant 2 nM RNA. Next, RIG-I displacement from the 5'ppp 10bp HP RNA (FAM) was monitored by changes in fluorescence polarization while titrating unlabeled 5'ppp ds39 RNA against 10 nM equimolar RIG-I-bound 5'ppp 10bp HP RNA (FAM). The Cheng-Prusoff equation was used to obtain 5'ppp ds39 RNA K_i values, which are representative of RIG-I's binding affinity for 5'ppp ds39 RNA (K_D). Data show means ± SD from 3 independent experiments. Statistical analysis was performed using unpaired t-test. *, $P<0.05$.
(C) ATPase activity of 1 μM WT and G731R RIG-I was measured on 5 nM 5'ppp ds39 RNA using a radiometric ATPase assay (biological replicates, n=3).
(D) Mant-ATP binding to WT and G731R RIG-I using fluorescence-based titration. The differences in the fluorescence intensity of Mant-ATP (F_M) and Mant-ATP with protein (F_{MP}) are plotted against Mant-ATP concentration. The error bars represent the standard error of the mean (n=3), and the curve shows the hyperbolic fit of the mean data to **equation 2** to obtain the Mant-ATP K_D values.
(E) ATPase activity of WT RIG-I with 5'ppp ds39 RNA was measured while titrating in increasing G731R protein. The error bars represent the standard error of the mean (n=3), and the curve represents fitting of the mean data to **equation 1** to obtain the IC_{50} value.

G731R is ATPase-deficient and competes with WT RIG-I for 5’ppp RNA binding

We next measured whether RNA binding stimulates the ATPase activity of G731R, as in WT RIG-I. The G731 residue lies within helicase motif VI, positioned between two critical arginine residues, R730 and R732, that coordinate ATP phosphates during catalysis (Figure 1C-D). Substitution of G731 with a bulky, positively charged arginine could perturb the position of the catalytic arginine, alter the local structure, or charge environment to affect ATP binding or hydrolysis. In the presence of 5′ppp ds39 RNA, WT RIG-I hydrolyzed ATP with a rate constant of 7.3 s^{-1}, whereas the ATPase rate of G731R was barely detectable (0.03 s^{-1}, Figure 4C).

Mant-ATP binding assays indicated that the ATPase defect is not due to impaired ATP binding. G731R bound Mant-ATP with a K_D of 14 μM, compared to 6.5 μM for WT RIG-I (P=0.0061) (Figure 4D). Given the intracellular ATP concentration of ~3 mM [26], this ~2-fold difference is unlikely to be physiologically relevant. Thus, while G731R can bind RNA and ATP, it is clearly defective in signaling, unlike the SMS mutants.

The cellular assays demonstrated that G731R suppresses WT RIG-I-dependent IFN-β signaling (Figure 3F-H), suggesting that the mutant interferes with WT RIG-I activation. Because G731R retains high-affinity binding to 5′ppp RNA but is signaling inactive, it may exert its dominant-negative effect by competing with WT RIG-I for viral RNA. To test this hypothesis, we measured the RNA-stimulated ATPase activity of WT RIG-I in the presence of increasing concentrations of G731R (Figure 4E). ATP hydrolysis by RIG-I is strictly dependent on RNA binding; therefore, WT ATPase activity provides a sensitive readout of productive WT-RNA complex formation. The addition of G731R reduced WT ATPase activity in a concentration-dependent manner, consistent with the progressive displacement of WT RIG-I from the RNA substrate. The IC_{50} value was consistent with the high-affinity binding of G731R to 5’ppp RNA. We did note that even a 20-fold molar excess of G731R did not completely abolish WT ATPase activity. This residual activity likely reflects a subpopulation of WT RIG-I molecules that remain engaged with the duplex stem of the 5′ppp ds39 RNA within mixed WT/G731R complexes.

The results indicate that G731R binds 5’ppp RNA with a high affinity and efficiently sequesters viral RNA from WT RIG-I. However, it cannot undergo the ATP-dependent conformational transition required for RIG-I activation. Consequently, G731R forms an RNA-bound, signaling-inactive complex that competitively suppresses WT RIG-I activation, providing a molecular explanation for its dominant-negative phenotype.

The G731R mutation prevents exposure of the CARDs-CHL upon RNA binding

The signaling inactivity of G731R is not due to a lack of ATPase activity by G731R, because SMS variants, such as C268F (motif I) and E373A (motif II), are ATPase-inactive and show a gain-of-function phenotype [9,19,21]. One explanation for the signaling inactivity of G731R could be that it binds 5’ppp RNA in an altered conformation that maintains the CARD domains in an autoinhibited state. To explore this hypothesis, we used hydrogen-deuterium exchange coupled to mass spectrometry (HDX-MS), a technique previously used to assess CARD exposure upon RNA binding [16,27-29]. HDX-MS measures the time-dependent exchange of backbone amide hydrogens with deuterium, detected by mass spectrometry. The rate of exchange reflects local protein structure: rapid exchange corresponds to unfolded regions, flexible loops, or solvent-exposed areas, whereas slow exchange indicates stably folded or buried regions. The time-consolidated differential HDX-MS patterns compare the conformational states of RIG-I with or without RNA, or between WT and mutant.

Differential HDX-MS comparing WT and G731R in the absence of RNA showed some differences, including decreased solvent exchange in CARD1 and the CHL of G731R (Figures 5A,B, S4-S6), and mild protection in the helicase and CTD domains of G731R, including helicase motif IVa (aa 661–681). Thus, G731R in the absence of RNA adopts a slightly more solvent-protected conformation than WT RIG-I.

The differential HDX-MS patterns of WT RIG-I with and without 5'ppp 10-bp hairpin RNA (Figures 5A, 5C, S7-S8, Table S5) revealed characteristics of RNA engagement and CARD domain exposure. The CARD domains (aa 1-186) and the CARD2:Hel2i interface, comprised by the CARD2-gate region (aa 138-156) (Figure 5C-i) and the Hel2i region (aa 556-578), showed increased solvent exchange in the presence of RNA. This is consistent with RNA binding disrupting the CARD2:Hel2i interface, leading to

CARDs exposure. Another small region of the Hel2i domain (aa 520-538), also part of the CARD2:Hel2i interface, was protected upon RNA binding, consistent with this Hel2i region forming a junction with the CTD (aa 895-915) [13,14,18]. Finally, we observed protection patterns throughout the Hel1 and Hel2 domains, coinciding with regions known to interact with the RNA backbone. Overall, these HDX patterns are consistent with RNA-induced conformational changes that expose CARDs in WT RIG-I.

The differential HDX-MS pattern of G731R with and without 5'ppp 10-bp hairpin RNA differed significantly from that of WT RIG-I. In contrast to the increased solvent exchange observed in the CARD domains of WT RIG-I upon RNA binding, G731R showed an overall protection of the CARDs and the CHL region (Figures 5A, 5D, S9-S10). The helicase domains showed protection consistent with RNA binding, but with a distinct pattern from that of WT RIG-I. Regions showing distinctly high protection included helicase motif IVa and the Hel2 loop (aa 661-693), as well as the capping loop (aa 842-855) in the CTD that interacts with the 5'ppp RNA end.

Overall, the HDX-MS suggests that the CARD and CHL regions of G731R are not exposed, despite RNA binding, consistent with the lack of signal transduction and the impaired IFN-β response. The distinct HDX-MS pattern indicates that G731R binds 5'ppp RNA in a conformation that differs substantially from the WT protein.

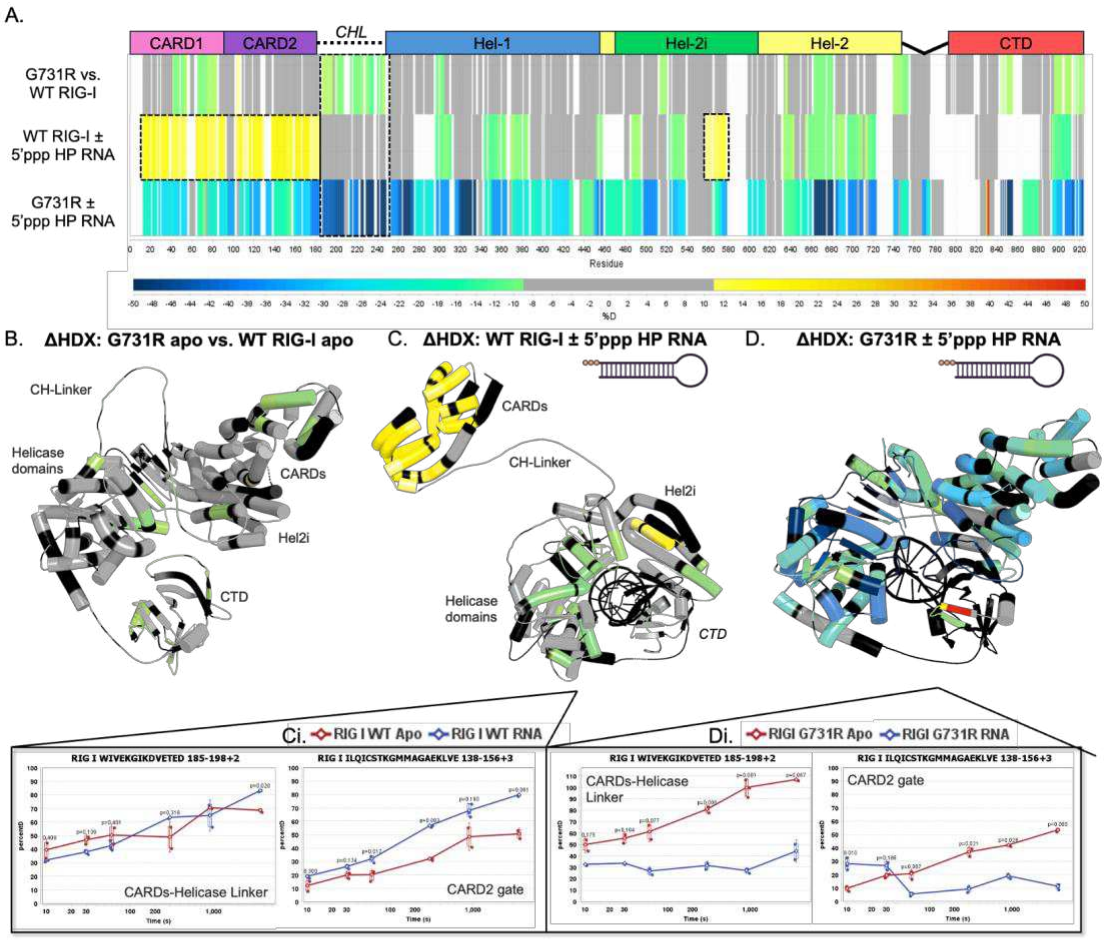


Figure 5. HDX-MS analysis of G731R reveals CARDs-CHL protection.
(A) Linear mapping of the HDX differential data of WT and G731R with and without 5'ppp HP RNA.
(B) The differential HDX pattern of G731R apo vs WT RIG-I apo mapped onto a 3D composite model of G731R apo (4A2W, 3TBK, 4AY2, & computationally modeled CARDs-Helicase Linker, (CHL).
(C) The differential HDX pattern of WT RIG-I ± 5'ppp 10bp HP RNA mapped onto a 3D composite model of RNA-bound WT RIG-I with CARDs exposed (PDB: 5E3H, 4P4H, 4AY2, & computationally modeled CHL. (i) Deuterium uptake plots of select RIG-I peptides represented as percent deuterium uptake over time.
(D) The differential HDX pattern of G731R ± 5'ppp 10bp HP RNA mapped onto a composite model of RNA-bound G731R with CARDs sequestered (PDB: 4A2W, 3TBK, 4AY2, & computationally modeled CHL. (i) Deuterium uptake plots of select RIG-I peptides represented as percent deuterium uptake over time.

A small deletion in the CHL partially rescues the activities of G731R

The protection of the intrinsically disordered CHL region in G731R in the presence of RNA was surprising. Previous studies have shown that CHL (aa 183-245) (Figure 6A) stabilizes the autoinhibited conformation of RIG-I [16]. Thus, 10 aa deletions within the CHL disrupt this regulation and increase the basal signaling response of RIG-I. We wondered if disrupting the CHL in G731R would rescue its activity. For this, we used the

well-characterized Δ190-200 RIG-I mutant. Consistent with previous findings, the Δ190-200 RIG-I showed a ~10-fold higher basal IFN-β signaling response than full-length WT RIG-I and a 2-fold higher 5'ppp ds39 RNA-stimulated response (Figure 6B). Interestingly, the 190-200 deletion in G731R increased both the basal and the 5'ppp RNA IFN-β response by 10-fold (Figure 6B, S1E). This indicates that disruption of CHL rescues the RNA response in G731R. This rescue is partial because the final RNA response of Δ190-200 G731R remained lower than Δ190-200 RIG-I.

Biochemically, deletion of the CHL and CARDs regions increased the ATPase function of G731R (Figure 6C). The ATPase rate of full-length G731R in the presence of 5'ppp ds39 was 240-fold slower than WT RIG-I, whereas the rate of CHL-CARDs deleted G731R HelCTD was only 12-fold slower than WT HelCTD. Together, these results indicate that the CARDs-CHL module, previously shown to stabilize the autoinhibited state of WT RIG-I [16], also plays a key role in stabilizing the inactive conformation of G731R, and that disrupting this gating system partially relieves its loss-of-function phenotype.

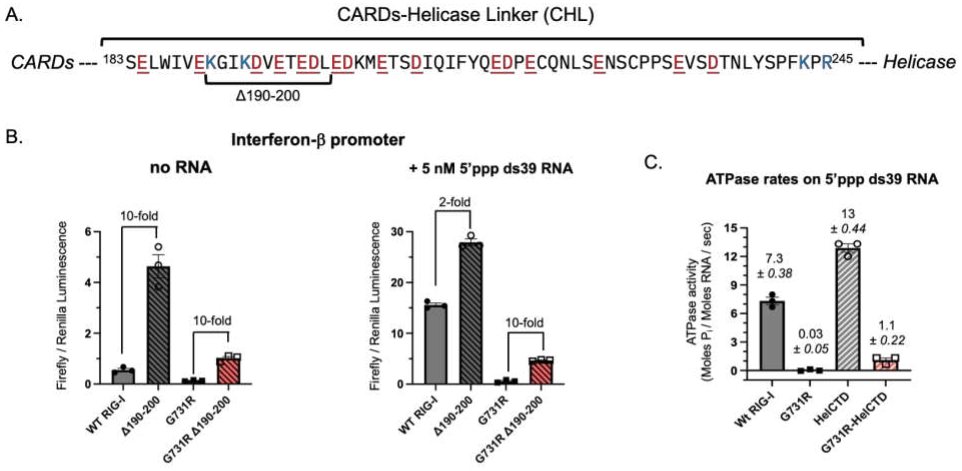


Figure 6. The role of CHL in G731R loss of function mechanism
(A) Amino acid sequence of the intrinsically disordered CHL of RIG-I. Negatively charged residues are colored red and underlined; positively charged residues are colored blue. The 190-200 segment is indicated.
(B) IFN-β promoter response of the 10 aa deletion in the CHL (Δ190-200) in WT and G731R RIG-I was measured by the dual luciferase reporter assay in the absence and presence of 5 nM 5'ppp ds39 RNA (independent RNA transfections, n=3). The fold-change between WT and Δ190-200 deletion is shown.
(C) ATPase activity of 1 μM protein on 5 nM 5'ppp ds39 RNA was measured using the radiometric ATPase assay performed three times (biological replicates, n=3). Mean rates of hydrolysis (Moles P_i / Moles RNA / sec) are reported, and the individual data points are plotted over bars representing the mean values with error bars representing the standard error of the mean (SEM).

G731R mutation traps RIG-I in a kinetically unstable "CTD-mode" conformation.

Previous stopped-flow kinetic studies showed that RIG-I forms two kinetically distinct 5′ppp RNA-end bound states defined by their distinct dissociation rates: a transient "CTD-mode" and a long-lived "Helicase-mode" [16,17]. Based on the kinetic and structural data, we proposed that the CTD-mode represents an initial intermediate in the RNA-binding pathway, wherein the flexible CTD of autoinhibited RIG-I rapidly captures the 5′ppp RNA terminus (Figure 7A). Transition to the Helicase-mode occurs when the helicase core closes around the RNA duplex while maintaining end-contacts via the CTD.

To determine whether the G731R mutation disrupts this conformational transition, we measured RNA dissociation kinetics using stopped-flow fluorescence studies (Figure 7B). Dissociation of WT RIG-I from the 5′ppp ds27 RNA (labeled with DY47 dye near the 5'ppp-end, Table S5) followed biphasic kinetics, with ~75% of molecules dissociating rapidly (lifetime ~7s, CTD-mode) and ~25% dissociating slowly (lifetime ~ 200s, Helicase-mode; Figure 7C-D). In contrast, G731R dissociation was dominated by the fast phase, with ~92% of the mutant molecules remaining in the CTD-mode (lifetime ~7s) and only ~8% populating the Helicase-mode (lifetime ~198s). The minor slow phase has a greater fitting variance due to its negligible amplitude.

ATP addition accelerated the dissociation rate of WT RIG-I from the 5'ppp RNA-end in the Helicase-mode by ~50%, consistent with ATP hydrolysis driving translocation away from the 5′ppp end, while leaving the CTD-mode lifetime unchanged (Figure 7C-D, Table S3). By contrast, ATP had no effect on either kinetic phase of G731R, consistent with its catalytic defect.

These kinetic results indicate that G731R binds 5′ppp RNA primarily in the kinetically unstable CTD mode. Together with our HDX-MS data demonstrating that the CARD domains remain sequestered in G731R, we propose that the mutation traps RIG-I in a short-lived, signaling-inactive intermediate that likely cannot support stable interactions with downstream partners to sustain signaling.

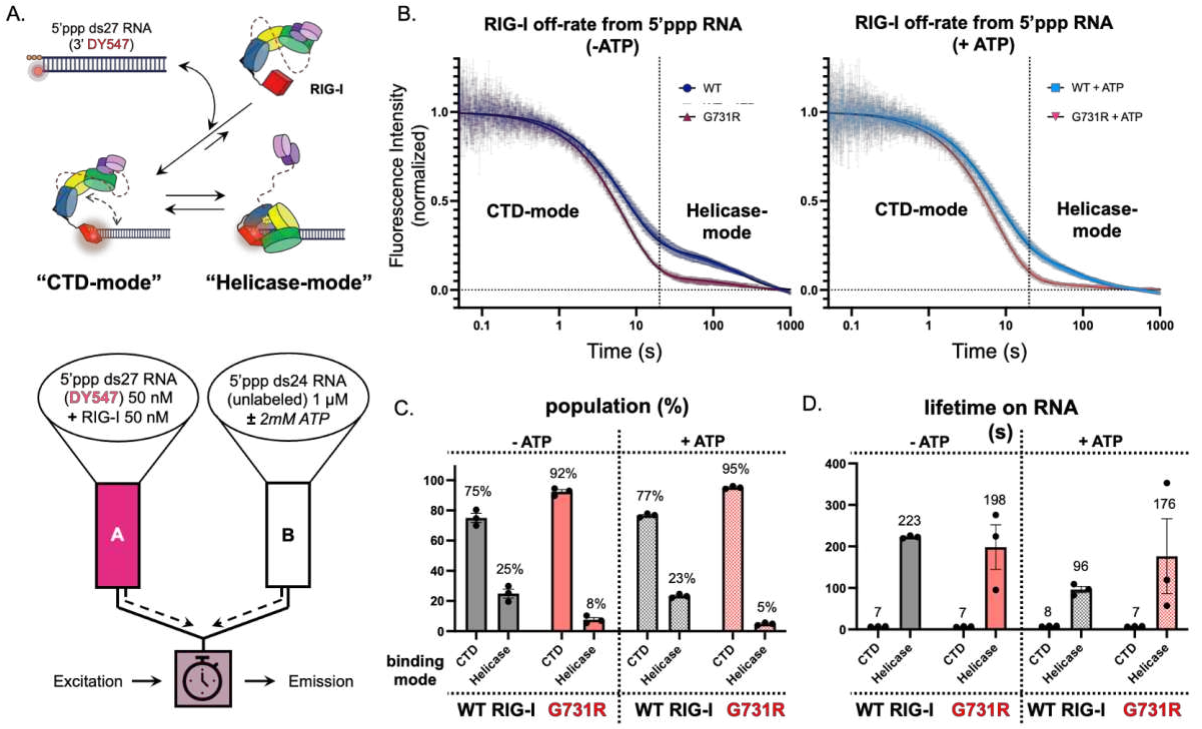


Figure 7. G731R is trapped in a kinetically unstable CTD-mode
(A) RIG-I forms kinetically distinguishable CTD-mode and Helicase-mode conformations on 5'ppp RNA. Experimental setup to measure the off-rate of RIG-I from 5'ppp RNA in a stopped-flow instrument.
(B) Biphasic kinetics of WT RIG-I and G731R dissociation from 5'ppp ds27 RNA with and without ATP. The time axis is shown on a log scale to clearly show the two phases. The dissociation kinetics (biological replicates, n=3) best fit to the sum of two exponentials (**equation 4**), providing slow and fast off-rates and the corresponding amplitudes.
(C) The fast (CTD-mode) and slow (Helicase-mode) phase amplitudes from data in panel C in the absence of ATP are shown as percent population and their lifetimes (1/off-rate). Three biological replicates are shown with SEM.
(D) The population and lifetimes of CTD-mode and Helicase-mode phases are shown in the presence of ATP. Three biological replicates are shown with SEM.

G731 substitutions lead to both loss-of-function and gain-of-function phenotypes

To investigate whether the loss-of-function phenotype of G731R is specific to the glycine to arginine mutation, we mutated G731 to lysine (K), glutamic acid (E), alanine (A), leucine (L), and phenylalanine (F), thereby examining the effects of varying side chain charge and size. IFN-β reporter assays revealed that bulky positively charged (G731K) and negatively charged (G731E) mutations resulted in loss-of-function phenotypes, while G731F showed partial activity (Figure 8A). By contrast, the small, uncharged G731A and G731L sidechains were fully active in the presence of 5'ppp ds39 RNA and, surprisingly, showed higher basal signaling than WT RIG-I, like the

gain-of-function SMS mutants of RIG-I. Thus, steric hindrance from bulky substitution at G731 may explain the conformational shift to the inactive state. Indeed, modeling using the PyMOL mutagenesis wizard predicted steric clashes between R731 and nearby beta strands in the Hel2 domain (aa 711-715, 737-742) when modeled into the ATPase-competent RIG-I structure (PDB: 4A36) (Figure 8B). Visually, there appears to be an inverse relationship between the degree of predicted steric hindrance (modeled in PyMOL) and IFN-β signaling activity, with bulky charged substitutions showing the greatest clashes and lowest signaling.

RIG-I is unique in containing one glycine flanked by two arginine fingers in Motif VI, whereas most other SF2 helicases contain a more hydrophobic alanine or valine at that position (Figure 1D). To understand the mechanistic basis of G731A's gain-of-function phenotype, biochemical studies were carried out on the mutant. In contrast to G731R, G731A retained normal RNA-dependent ATPase activity (Figure 8C). Fluorescence polarization experiments showed that G731A has a similar affinity for 5'ppp RNA compared to WT RIG-I (1.1 nM and 1.2 nM K_D, respectively) (Figure 8D). However, G731A showed a threefold tighter affinity for ds26 Stem RNA compared to WT RIG-I (1.7 μM versus 4.9 μM K_D) (Figure 8E). The ds26 Stem RNA lacks 5'ppp and RNA blunt ends, thus mimicking stem regions in self RNAs. The HDX-MS analysis of G731A shows a similar conformation as WT RIG-I in the absence of RNA (Figures S4 and S11) and CARDs exposure in the presence of RNA comparable to WT RIG-I (Figures S4 and S12), in marked contrast to the CARD-protected state observed for G731R (Figure S4).

These biochemical results suggest that, despite retaining normal ATPase activity, the G731A mutation increases nonspecific dsRNA binding, thereby promoting elevated basal signaling. Although this phenotype resembles that of the ATPase-deficient SMS mutants, it likely arises through a distinct molecular mechanism that remains to be elucidated.

Together, our findings identify the evolutionarily conserved G731 as a critical regulator of the ATP-dependent conformational transitions that couple viral RNA recognition to antiviral signaling. More broadly, they demonstrate that distinct amino acid substitutions at a single residue can produce fundamentally different functional

outcomes, identifying G731 as a conformational switch that finely tunes RIG-I activity. These observations underscore the importance of experimentally validating disease-associated variants rather than relying solely on computational pathogenicity predictions.

The loss-of-function G731R variant identified in our patient is novel, whereas another substitution at the same position, G731E, which we also found to be loss-of-function, is present in a single individual of unknown clinical status in gnomAD (v4.1.0). In contrast, the gain-of-function substitutions G731A and G731V have not been reported in human population databases. Although all G731 substitutions receive high CADD scores (>20), AlphaMissense, which incorporates evolutionary conservation and structural context [30], assigns substantially lower pathogenicity scores, classifying G731A (score 0.308) as likely benign (Table S4). This prediction contrasts with our experimental data that G731A has a gain-of-function phenotype characterized by elevated basal signaling (Figure 7B). Together, these findings highlight the limitations of current pathogenicity prediction algorithms for residues that regulate protein conformational dynamics and emphasize the indispensable role of mechanistic and biochemical studies in interpreting rare human variants.

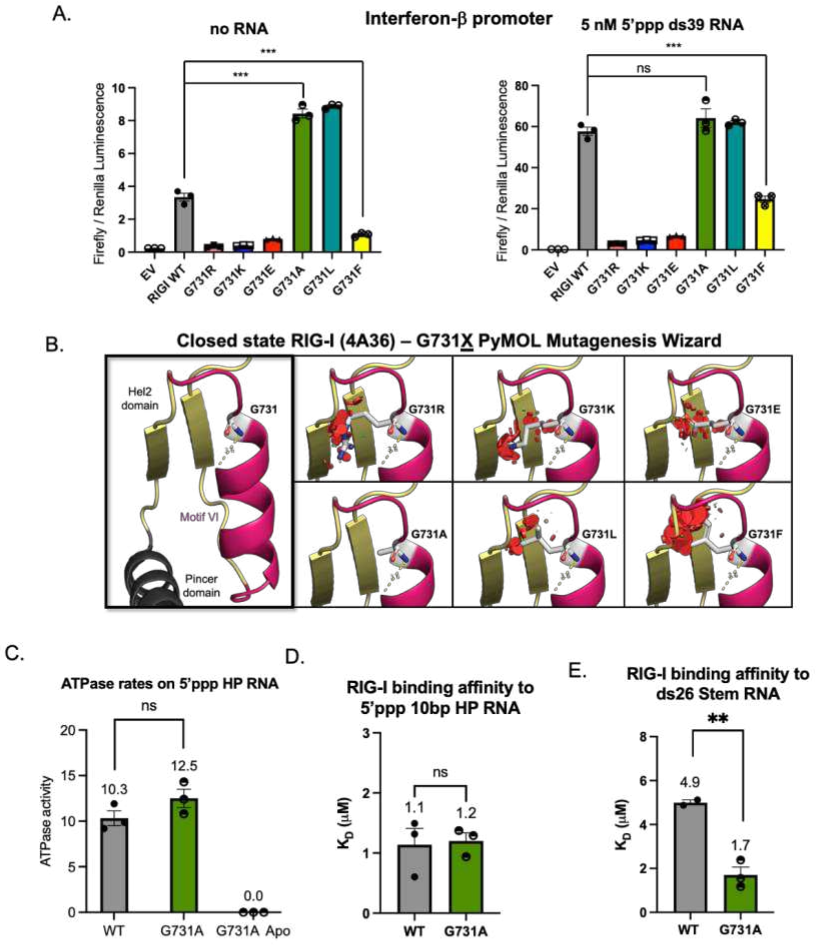


Figure 8. The G731 mutation leads to both loss and gain of function.
(A) IFN-β response of various G731X mutants with and without RNA was measured by dual luciferase reporter assay (independent RNA transfections, n=3).
(B) PyMOL Mutagenesis Wizard analysis of various G731X mutations in the closed state of RIG-I (4A36). The visible disks indicate pairwise overlap of atomic van der Waals radii.
(C) ATPase activity of 50 nM WT and G731A was measured with and without 5 nM 5'ppp 10bp HP RNA (biological replicates, n=3).
(D) 5'ppp 10bp HP RNA binding affinity (K_D) of WT and G731A was obtained using fluorescence polarization titrations of RIG-I against constant 2 nM RNA (biological replicates, n=3).
(E) ds26 Stem RNA binding affinities of WT and G731A were obtained by measuring ATPase activity at various RIG-I concentrations against a constant 200 nM ds26 Stem RNA. The K_D values obtained from the binding curves are plotted. Note that only two points are shown for WT as a K_D could not be obtained from one of the curves (biological replicates, n=2). Three points are shown for G731A (biological replicates, n=3).

Together, these findings suggest that bulky, charged substitutions at G731 trap RIG-I in a CARD-protected, signaling-inactive CTD-mode intermediate, preventing its ATP-dependent transition to the signaling-competent helicase-bound state (Figure 9). In contrast, smaller substitutions lower the barrier for domain closure, promoting productive duplex engagement and RIG-I activation.

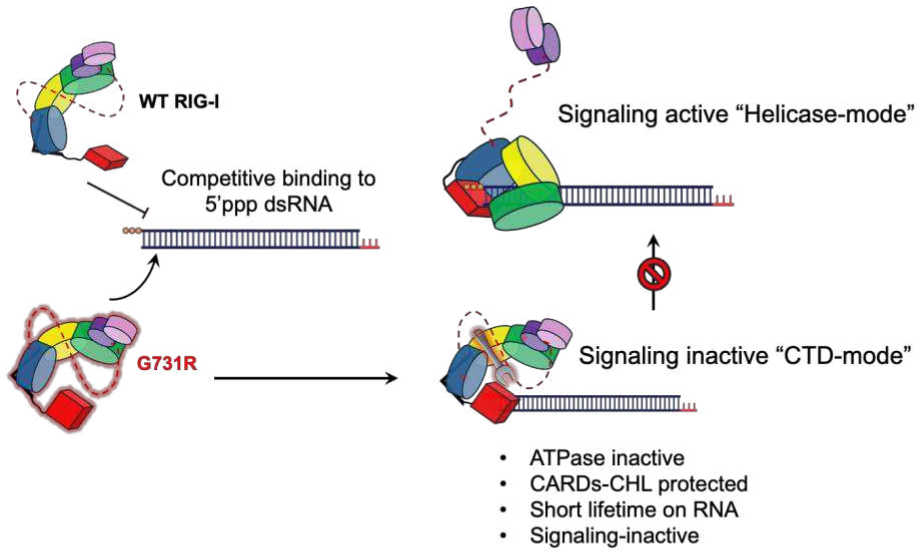


Figure 9. Model of dominant-negative loss of function activity of G731R RIG-I
Mechanistic model of G731R mutation trapping RIG-I in the CTD-mode RNA-bound conformation, preventing CARDs-CHL exposure, and competitively interfering with wild-type activity.

DISCUSSION

Here, we identify the first naturally occurring dominant-negative loss-of-function RIG-I variant affecting a conserved helicase motif and define its molecular mechanism of action. Originating from a broader genetic investigation of rare deleterious RIG-I variants in patients with severe COVID-19, this study elucidates how the G731R mutation produces a dominant negative phenotype and how different mutations at this residue can produce opposite phenotypes. Like the constitutively active SMS variants, with mutations in helicase motifs I and II. G731R retains high-affinity binding to viral RNA and lacks ATPase activity. However, unlike SMS mutants, G731R becomes trapped in an RNA-bound, signaling-incompetent intermediate that competitively inhibits WT RIG-I. These findings demonstrate that ATPase deficiency alone does not determine RIG-I activity and challenge the prevailing view that viral RNA binding is sufficient for RIG-I activation. Our work indicates that, in addition to proofreading, ATP-dependent conformational changes serve as checkpoints that link viral RNA recognition to productive signaling.

Mutations such as G731R, which stabilize transient intermediates along the RNA-activation pathway (Figure 9), provide a unique tool to capture structural states that are otherwise inaccessible. Our findings support a model in which viral RNA binding first

generates a high-affinity CTD-bound intermediate. Rather than proceeding through normal helicase closing, G731R uniquely traps RIG-I in this initial CTD mode, providing insights into this state and proving that the CTD mode alone is signaling-inactive (Figure 9). Productive activation requires an ATP-dependent structural transition from the CTD mode into a fully closed helicase mode at the Hel1-Hel2 interface. While SMS mutations (e.g., C268F, E373A) permit this structural transition and become trapped in long-lived, signaling-competent states due to impaired ATP hydrolysis, the G731R substitution disrupts this transition. Glycine 731 lies directly between the two catalytic arginine fingers of helicase motif VI at the Hel1-Hel2 interface. Replacing this conserved glycine with a bulky arginine likely disrupts motif VI folding and prevents productive closure of the helicase core (Figure S13), thereby stabilizing an RNA-bound, signaling-incompetent intermediate. Thus, viral RNA recognition and receptor activation are functionally separable events, establishing the CTD-to-helicase mode transition as a critical checkpoint governing signal transduction.

Remarkably, substituting G731 with alanine or leucine produces the opposite phenotype: increasing basal signaling while preserving ligand-induced activation. Evolutionary alignment reveals that while motif VI is conserved across SF2 helicases, an intervening glycine between the arginine fingers is a RIG-I-specific feature (Figure 1D); most SF2 helicases and RLR family members (MDA5, LGP2) contain an alanine or valine. Thus, glycine plays a distinct regulatory role in RIG-I, and subtle perturbations at this position can shift the conformational equilibrium toward either signaling-competent or signaling-incompetent states. This demonstrates that key residues in conserved helicase motifs act as dynamic structural switches rather than static catalytic elements.

Studies of inborn errors of immunity have established the essential role of the type I IFN pathway in human host defense [31,32]. While partial RIG-I defects predispose individuals to severe influenza and acute hepatitis E virus infections [33-35], severe human RIG-I deficiency remains extraordinarily rare, with naturally occurring heterozygous variants typically retaining substantial residual activity. Only a single case of complete biallelic loss-of-function was reported in a patient with Kaposi's sarcoma-associated herpesvirus [36]. Our identification of the heterozygous G731R variant in a patient presenting with severe COVID-19 establishes that dominant-negative inhibition by a

single allele can severely compromise human innate immunity. Biochemically, G731R acts as an RNA competitor to WT RIG-I, severely impairing both type I IFN production and control of virus replication in patient-derived immune cells and co-expression models. This clinical manifestation in a COVID-19 patient is particularly noteworthy given that MDA5 is widely recognized as the primary sensor of SARS-CoV-2 in vitro [37-39]. The profound susceptibility observed here aligns with emerging evidence that RIG-I and MDA5 act cooperatively in vivo [40-42], demonstrating that RIG-I plays an essential, non-redundant role in human host defense against SARS-CoV-2.

These newly defined regulatory checkpoints present attractive targets for therapeutic intervention. The observation that deletion of the CHL partially rescues G731R signaling suggests that targeting the CHL or helicase motifs with small molecules or peptides could fine-tune RIG-I activity. In heterozygous patients carrying dominant-negative variants, therapeutics might overcome competitive inhibition by using RIG-I agonists that mimic SMS variants, thereby driving WT RIG-I activation and restoring antiviral immunity. Beyond therapeutic design, these observations highlight the persistent challenges of interpreting patient-derived variants. As reported for disease-associated STAT3 mutations [43], different amino acid substitutions at the same residue can yield markedly different biochemical and functional consequences, underscoring the necessity of experimental validation alongside computational prediction. Indeed, despite its high CADD score and clear gain-of-function phenotype, G731A was classified as benign by AlphaMissense (Table S4). Such distinctions not only underscore the need for tailored treatment approaches in genetically variable patients but also highlight the plasticity of RIG-I modulation, whether through activation or suppression, at regulatory checkpoints within its biochemical activation pathway.

Limitations

HDX-MS revealed the conformational changes associated with G731R dysfunction, while stopped-flow kinetics suggested that the signaling-inactive state corresponds to the CTD-mode intermediate. However, these approaches do not provide the atomic-resolution structural information needed to define this conformation. Furthermore, although our studies show that distinct substitutions at G731 produce opposing

functional outcomes, the structural basis of the gain-of-function phenotype of G731A remains unresolved. Future structural and biophysical studies of G731R and G731A will provide atomic-level insight into the signaling-inactive conformation of G731R and reveal how helicase motif VI regulates the ATP-dependent conformational transitions that govern RIG-I activation.

Data and code availability

- The raw data acquired in this study has been deposited at Mendeley Data (https://data.mendeley.com/preview/bc5v94g8ht?a=a1349b1f-b329-4a3c-b4e7-77dd933b6493) and are publicly available as of the date of publication.
- The patient's whole-genome sequencing dataset was deposited in dbGaP under accession number phs002245.v1.p1, which is a controlled access database for qualified investigators.
- No original code has been generated for this publication.
- Any additional information required to reanalyze the data reported in this paper is available from the lead contact upon request.

Materials availability

- The plasmids used in this study will be made available on request. Patient samples are available through A.L. through a material transfer agreement for human materials from the University of Bari Aldo Moro.
- Further information and requests for resources and reagents should be directed to and will be fulfilled by the lead contact, Smita Patel (patelss@rutgers.edu).

Acknowledgements

We thank the patient for participating in this research study, Dr. Andrew Snow for scientific discussions and critical comments on the manuscript, and Mary Magliocco for technical assistance. This work was supported by the National Institute of General

Medical Sciences (NIGMS) [GM118086 to S.S.P.], the Intramural Research Programs of the National Institute of Allergy and Infectious Diseases [1ZIAAI001265 to H.C.S.], [1ZIAAI001383 to J.M.], [1ZIAAI001312 to S.M.H.]. The contributions of the NIH authors were made as part of their official duties as NIH federal employees, are in compliance with agency policy requirements, and are considered Works of the United States Government. However, the findings and conclusions presented in this paper are those of the authors and do not necessarily reflect the views of the NIH or the U.S. Department of Health and Human Services.

Author contributions

Conceptualization, M.S., H.J., W.T., P.R.G., J.M., H.C.S., S.S.P.; Methodology, M.S., H.J., E.G., S.J.N., P.G., H.C.S., S.S.P.; Formal Analysis, Y.Z.; Investigation, M.S., T.M., H.J., E.G., S.J.N., B.D.P., W.T., P.H., C.A., B.K., A.S., P.L., A.V., I.A.I., E.R.S., L.B.R., C.L.S.; Resources, A.S., P.L., A.L.; Writing, - Original Draft, M.S., H.J., H.C.S., S.S.P.; Writing – Review and Editing, M.S., H.J., W.T., P.H, J.M., H.C.S., S.S.P.; Visualization, M.S., H.J., Y.Z.; Data Curation, M.S., B.D.P., Y.Z.; Supervision, S.M.H., C.L.D., H.C.S., S.S.P.; Project Administration, A.L., H.C.S.; Funding Acquisition, J.M., H.C.S., S.S.P.

Ethics declarations

Competing interests

The authors declare no competing interests.

METHODS

Patient Information and Laboratory Evaluation

The patient, a 63-year old Caucasian male, was hospitalized in early Spring of 2020 with critical COVID-19 pneumonia. He had neither comorbidities nor a previous history of severe viral infections, nor any family history of virus-associated diseases. He

presented with a nine-day history of worsening fever, cough, and dyspnea. Radiological evaluation in the emergency department revealed diffuse lung infiltrates, and a nasopharyngeal swab molecular assay was PCR positive for SARS-CoV-2. Despite treatment with azithromycin, hydroxychloroquine, and lopinavir/ritonavir, he required invasive mechanical ventilation for acute respiratory distress, as well as therapeutic anticoagulation with low molecular weight heparin (LMWH) for incidental thromboembolic complications. After ten days in the intensive care unit (ICU), he was transferred to the inpatient service and stayed for a total of 34 days before hospital discharge. Subsequently, he received influenza and COVID-19 immunizations and has not developed any new infectious complications.

During his hospitalization, the patient had elevated CRP (147 mg/L), unremarkable polymorphonuclear leukocyte counts (5.305 x 10^9/L, normal range 4.0-11.3 x 10^9/L), and decreased lymphocyte numbers (0.449 x 10^9/L, normal range 1.320-3.600 x 10^9/L). Autoantibodies against type I IFNs (IFN-α2, IFN-β, or IFN-ω), which can neutralize endogenously produced type I IFNs to increase COVID-19 disease severity[44,45], were not detected in the patient's plasma (106, 254, 326 fluorescence intensities, well below the normal cutoffs of <1,310, <386, and <1,387 fluorescence intensities for anti-IFN-α2, anti-IFN-β, and anti-IFN-ω autoantibodies, respectively).

The patient provided written informed consent for his enrollment and participation in research protocol 1563 (Bari, Italy), which was approved by the local institutional review board (IRB). He was classified as critically ill according to the Diagnosis and Treatment Protocol for Novel Coronavirus Pneumonia based upon the following criteria[46]: mechanical ventilation (CPAP, BiPAP, intubation, hi-flow oxygen); or septic shock; or organ damage requiring admission in the ICU; or severe patients with oxygen saturation at rest 93% or lower OR respiratory rate >30/min OR PaO2/FiO2 <300.

Genetic Analysis

Genomic DNA was extracted from frozen whole blood from the patient. Whole genome sequencing was performed using Illumina NovaSeq 6000 sequencing system (Illumina). All sequencing reads were aligned with hg19 genome assembly with

Burrows–Wheeler Aligner (BWA) and the variant calling were done by the Genome Analysis Toolkit (GATK) best-practice pipeline.

To confirm the *RIG-I* mutation in the patient, genomic DNA was isolated from the patient's blood leukocytes and amplified by PCR using forward primer 5′-ACCAGCATTACTAGTCAGAAGGA -3′ and reverse primer 5′-ACAGCTCAACTTTCCTGGGA -3′, followed by Sanger dideoxy sequencing from both directions.

Autoantibodies testing

Serum samples from the patient were screened for autoantibodies against IFN-α, IFN-β, and IFN-ω using a multiplex particle-based assay, as previously described[47]. Using this methodology, the cutoff values (mean ± 3 standard deviations) for healthy donors serving as negative controls (n=1099) are fluorescence intensities on the Luminex machine of <1,310, <386, and <1,387 for anti-IFN-α, anti-IFN-β, and anti-IFN-ω autoantibodies, respectively.

Plasmids and mutagenesis

Human *RIG-I* cDNA corresponding to NCBI reference sequence NM_014314.3 was purchased from SinoBiological (clone HG17547-U) and subcloned into pcDNA3.1 (ThermoFisher) or pLV-EF1a-IRES-Puro (Addgene). The G731R mutant was generated by site-directed mutagenesis through PCR amplification of full-length plasmids encoding WT RIG-I with a primer pair containing the corresponding mutation as previously described[48].

Cells

For complete medium, DMEM or RPMI 1640 (ThermoFisher) was supplemented with final concentrations of 10% FBS (Gemini or Atlanta Biologicals), 2 mM L-glutamine, 100 IU/mL penicillin, 100 µg/mL streptomycin (all from ThermoFisher), and 55 µM 2-mercaptoethanol (MilliporeSigma). Human peripheral blood mononuclear cells (PBMCs) were isolated from the blood of patients and healthy donors by Ficoll-Paque density gradient centrifugation (Cytiva). Monocytes were isolated from PBMCs using $CD14^+$ microbeads (Miltenyi Biotec). Monocyte-depleted PBMCs were stimulated with anti-

human CD2/CD3/CD28 beads (Miltenyi Biotec) according to the manufacturer's instructions and cultured in complete RPMI medium supplemented with 100 U/mL recombinant human IL-2 (Aldesleukin, Prometheus) to expand T cells for 2 weeks before use.

Monocytes were either cultured overnight in complete RPMI medium (1×10^6 cells/mL) supplemented with 50 ng/mL M-CSF prior to use in experiments or differentiated into monocyte-derived dendritic cells (MoDCs). For MoDC generation, 2×10^6 monocytes were seeded into 6-well plates containing 2 mL of complete RPMI medium supplemented with 50 ng/mL GM-CSF, and 50 ng/mL IL-4. Cells were replenished every other day with 1 mL of fresh medium containing 50 ng/mL GM-CSF and 50 ng/mL IL-4. MoDCs were harvested on day 7 and used to assess type I interferon (IFN-I) responses following stimulation with RIG-I agonists.

Human primary dermal fibroblasts were isolated from a skin biopsy obtained from a healthy donor, as previously described [48]. Fibroblasts were immortalized by lentiviral transduction with human telomerase reverse transcriptase (hTERT) (Applied Biological Materials). hTERT-immortalized dermal fibroblasts were maintained in complete DMEM medium.

RIG-I KO hTERT fibroblasts were generated by using the CRISPR Cas9/RNP system as previously described[49]. Briefly, guide RNA (gRNA) was prepared by mixing 10 µL target gene specific CRISPR RNA (crRNA, 100 µM) and 10 µL tracrRNA (100 µM) followed by heating to 95 °C and slowly cooling to room temperature. Cas9/RNP was prepared by incubating 10 µL gRNA (500 pmol) with 200 pmol of Cas9 protein at room temperature for 10 minutes. Cas9/RNP complexes were transfected into fibroblasts (0.2 million cells resuspended in 20 µl P3 nucleofection solution) using the 4D Nucleofector system (Lonza) program DT-130. The three different RIG-I crRNA used were *RIG-I* crRNA-1, 5'-AATTCCCACAAGGACAAAAG-3'; *RIG-I* crRNA-2, 5'-AGGTTGTTCACAAGAATCTG-3'; *RIG-I* crRNA-3, 5'- GGCATCCCCAACACCAACCG-3'.

To reconstitute RIG-I KO fibroblasts with RIG-I variants, lentivirus particles expressing RIG-I WT or G731R were generated as previously described[49]. *RIG-I* KO

hTERT fibroblasts were seeded at 0.2 million cells per well in a 6-well plate, transduced first with WT RIG-I or G731R lentivirus particles and selected with 1 μg/mL puromycin (ThermoFisher) for 3 days after transduction to establish cell lines stably expressing RIG-I WT or G731R. Cells stably expressing WT RIG-I were reseeded into 12-well plates (0.2 million per well) and then transduced with lentivirus either expressing G731R or empty lentivector (EV). The expression levels of RIG-I were analyzed by qRT-PCR. The relative expression of RIG-I WT and G731R in the sequentially transduced cells was assessed by cDNA sequencing as described in the "RT-PCR" section below.

Cell stimulation with intracellular RIG-I agonists

Human hTERT fibroblasts, monocytes, monocyte-derived dendritic cells (MoDCs), and cultured T cells were stimulated with the intracellular RIG-I ligands 5′ppp-ds39 RNA (in vitro transcribed)[50] or 3p-hpRNA (InvivoGen) at the indicated doses using a 4D Nucleofector system (Lonza). Cells were transfected under the following conditions: hTERT fibroblasts (0.2×10^6 cells in 20 μL P2 buffer, program DT130), monocytes (0.2×10^6 cells in 20 μL P3 buffer, program EA100), MoDCs (0.2×10^6 cells in 20 μL P3 buffer, program CB150), and T cells (1×10^6 cells in 20 μL P3 buffer, program EO115). Following transfection, cells were transferred to 12-well plates containing 2 mL of the appropriate complete culture medium per well and incubated for 3 hours. Total RNA was then isolated, and *IFNB1* transcript levels were quantified by qRT-PCR.

hPIV infections

In some experiments, hTERT-fibroblasts were infected with hPIV3-eGFP, a recombinant human parainfluenza virus type 3 (hPIV3) derived from the JS strain and expressing enhanced green fluorescent protein (eGFP) as previously described [51]. In brief, hTERT fibroblasts were seeded at $1x10^5$ cells per well in a 12-well plate in complete DMEM. After overnight culture, cells were infected with hPIV3-eGFP at a multiplicity of infection (MOI) of 0.2, based on $2x10^5$ cells per well at time of infection. Cells were harvested at 24 to 48 hours post-infection for flow cytometric analysis of GFP expression in viable cells.

Interferon-β Reporter cell signaling assays

HEK293T RIG-I$^{-/-}$ cells were grown at 5% CO_2 and 37°C in 2 mL of DMEM with 10% FBS to 70% confluency and co-transfected with 500 ng firefly luciferase reporter plasmid (pLuc125), 100 ng renilla luciferase plasmid (pRL-TK), and 50 ng of a plasmid carrying either the WT RIG-I gene or mutant construct under the constitutively active CMV promoter (pcDNA 3.1) or EF1-α promoter (pEF-BOS), as indicated in the text. The firefly luciferase gene is under the control of the interferon-β promoter, and the renilla luciferase plasmid is under the control of the constitutively active TK promoter. The plasmid transfections were performed with X-tremeGENE HP DNA Transfection Reagent (Roche). Cells were replated in 96-well plates the next day at 250,000 cells/mL density and transfected with 0, 5, or 50 nM 5'ppp ds39 RNA using Lyovec transfection reagent (InvivoGen). After 20 hours, the activities of firefly and renilla luciferases were measured sequentially with the Dual-Luciferase Reporter Assay System (Promega). Data was collected in triplicate sets, and a ratio of firefly to renilla luciferase activity were calculated to indicate relative interferon expression levels. Competition assay was performed by titrating CMV-G731R plasmid against 50 ng EF1-α WT RIG-I in the presence or absence of 5 nM 5'ppp ds39 RNA. Total plasmid concentration was kept constant by substitution with empty vector. The ratio of firefly to renilla (Y) were plotted against G731R plasmid (X) concentration. The inverse hyperbolic dependence was fit to equation 1 to obtain the half maximal inhibitory concentration (IC_{50}). Top represents the Y-intercept in the absence of G731R inhibition, and Bottom represents the baseline of signaling at maximum inhibition.

Equation 1: $$Y = \text{Bottom} + \frac{\text{Top}-\text{Bottom}}{\frac{X}{IC50}+1}$$

In some experiments, 293T cells were seeded at 100,000 cells per well in 48-well plates one day prior to transfection. Cells were transiently transfected using Lipofectamine 2000 (Invitrogen) with firefly luciferase reporter plasmid driven by human IFN-β promoter (100 ng) and a constitutively expressed Renilla luciferase reporter plasmid (10 ng) together with WT or G731R RIG-I constructs (20 ng). Six hours after transfection, cells were infected with hPIV (MOI 3) and cultured for an additional 20 hours before cell lysis for Luciferase activity. Dual luciferase activities were measured according to the manufacturer's protocol (Promega) using a microplate reader (BMG

Labtech Fluostar Omega). Firefly luciferase activity for G731R was normalized to Renilla Luciferase activity and then reported as fold change relative to WT. To test for the dominant negative effect of G731R on WT RIG-I, 293T cells were co-transfected with either EV or G731R constructs (5 to 20 ng), along with RIG-I WT (5 ng) for 6 hours. Luciferase activity was induced by infecting cells with hPIV (MOI 3) and lysing them 20 hours later. Firefly luciferase activity was first normalized to Renilla luciferase activity and then shown as fold change relative to EV.

Western Blots

For each sample, total protein lysates were prepared by pelleting and lysing 250,000 cells in 40 µL of 2× SDS sample buffer (62.5 mM Tris, pH 6.8, 1% SDS, 15% glycerol, 2% β-mercaptoethanol, and 0.005% bromophenol blue) and then boiled for 10 min. Proteins were separated by SDS PAGE and transferred onto 0.2 µm PVDF membranes. The membranes were blocked with 5% nonfat milk in 1X PBST and immunoblotted with 1:500 anti-RIG-I (CST D14G6 Rabbit mAb #3743S) and 1:3000 anti-actin (CST 8H10D10 Mouse mAb #3700S) antibodies at 4°C overnight. After washing, membranes were immunoblotted with HRP-conjugated secondary antibodies (1:10,000, goat anti-rabbit (RIG-I) or goat anti-mouse (β-actin) IgG) for 1 hour. Blots were developed by using ECL western blotting substrate (ThermoFisher, Pierce) on a BioRad ChemiDoc system. In some experiments, protein lysates were from either 293T cells transfected with equal amounts of RIG-I WT or G731R plasmids or T cells cultured from the patient or normal donors, untreated or treated with 100 IU/mL recombinant human IFN-alpha-2b (Intron A; Merck) for 18 hours; in these experiments, lysates were separated on 3–8% Tris-Acetate gels and then transferred to nitrocellulose membranes using the TransBlot Turbo system (Bio-Rad). Membranes were blocked with 5% non-fat dry milk in PBST, then incubated overnight with anti-RIG-I antibody (1:1000; Proteintech, 20566-1-AP). After washing, membranes were incubated with HRP-conjugated goat anti-rabbit secondary antibody (1:10,000; Jackson ImmunoResearch), and signals were detected using ECL Western blotting substrate. Membranes were subsequently re-probed with anti-β-tubulin antibody (1:1000; Cell Signaling Technology, #2146), followed by the appropriate HRP-conjugated secondary antibody for signal detection.

qRT-PCR and cDNA sequencing

Total RNA from cultured cells was extracted using RNeasy Plus Kit (Qiagen). Reverse transcription was performed using the Maxima First Strand cDNA Synthesis Kit (ThermoFisher). Quantitative (q)RT-PCR was performed with PowerUp SYBR Green Master Mix (Thermo Fisher) on a 7500 Real Time PCR System (ThermoFisher). Target gene expression was normalized to *ACTB* expression, and then shown as fold-changes relative to the average levels in unstimulated cells or other controls as indicated in individual figure legends. Primer

sequences for RT-PCR were as follow: *IFNB1* forward primer 5'-AGGATTCTGCATTACCTGAAGG -3', *IFNB1* reverse primer 5'-GGCTAGGAGATCTTCAGTTTCG -3', *RIG-I* forward primer 5'-TGGCATATTGACTGGACGTG-3', *RIG-I* reverse primer 5'-CACTGGCTTTGAATGCATCC-3',*ACTB* forward primer 5'-ACCTTCTACAATGAGCTGCG-3', and *ACTB* reverse primer 5'-CCTGGATAGCAACGTACATGG-3'.

In some experiments, the relative expression of RIG-I WT and G731R alleles in patient's cells or fibroblasts transduced with RIG-I variants were assessed by PCR amplification of cDNA using forward primer 5'-GATTGCCACCTCAGTTGCTG-3', and reverse primer-5'-TCCCATGTCTGAAGGCGTAA-3', followed by Sanger dideoxy sequencing from both directions.

Protein expression and purification

RIG-I constructs were cloned into the protein expression vector pET28 SUMO and expressed as SUMO fusion proteins in *Escherichia coli* strain Rosetta (DE3) (Novagen)[13]. The soluble fraction was purified through a HisTrap HP column (GE Healthcare), followed by Ulp1 protease digestion to remove the 6x His-SUMO tag. The filtered soluble fraction was further purified through a heparin Sepharose column (GE Healthcare) to remove any contaminating nucleic acid. The purified protein was dialyzed into 50 mM HEPES pH 7.5, 50 mM NaCl, 5 mM $MgCl_2$, 5 mM DTT, and 10% glycerol overnight at 4^{o}C, and finally passed through a Superdex 200 10/300 Increase size

exclusion column (GE Healthcare) before being snap frozen in liquid nitrogen and stored at -80°C.

RNA synthesis by *in vitro* transcription

5' triphosphate 39-mer ssRNA was transcribed *in vitro* using a bacteriophage T7 RNA polymerase system[50]. 400 µl transcription reactions were run for 3 h at 30°C after mixing the required reaction components, including 250 mM HEPES pH 7.5 buffer, 30 mM $MgCl_2$, 40 mM DTT, 2 mM spermidine, 5 µg inorganic pyrophosphatase, 50 U RNasin, 2 µM dsDNA promoter and template sequence, 5 mM ATP, GTP, and UTP, and 1 µM T7 RNA polymerase, purified as previously described[52]. Reactions were quenched with 75 mM EDTA. The 39-mer ssRNA products were purified by gel electrophoresis on 1.5 mm × 30 cm 40% acrylamide and 6 M urea gel in 1.5xTAE. Electrophoresis was conducted at 500 V for 4 h, and the resulting ssRNA was identified by UV shadowing, the band was excised, and RNA was extracted from the gel using a Whatman Elutrap electroelution system in 1.5x TAE buffer run at 150 V for 6 h. The resulting ssRNA was concentrated with ethanol precipitation and stored at –80°C. The 39-mer ssRNA was analyzed for purity using LC–MS (Novatia, LLC; Newton, PA).

The 5'OH complementary fluorescent, or non-fluorescent, ssRNA was chemically synthesized (Dharmacon). Fluorescein-labeled 5'ppp 10bp HP RNA was chemically synthesized (TriLink).

Electrophoretic Mobility Shift Assay (EMSA)

EMSAs were performed by incubating 0, 20, 40, and 80 nM WT RIG-I or G731R variant with 20 nM 5'ppp ds39 RNA in ATPase buffer (50 mM MOPS pH 7.4, 5 mM DTT, 5 mM $MgCl_2$, 0.01% Tween20) for 30 minutes at 4°C. 2 mM ATP was optionally added to each reaction 15 min before loading the sample into the gel. 3 µl loading buffer (15% Ficoll 400 in Tris-borate buffer, pH 8.0) was added to the samples prior to loading on a 4–16% gradient Native PAGE gel (Invitrogen) and run at 4°C. Gels were scanned at 532 nm using a Typhoon FLA 9500 laser-based scanner (GE).

Fluorescence-based intensity and polarization RNA-binding assays

Fluorescence intensity and polarization measurements were performed on a Tecan Spark microplate reader in a 384-well black plate at 25°C. A monochromator was set to 485 nm for excitation and 535 nm for emission, with a 20 nm bandwidth. To measure 5'ppp 10bp HP RNA binding affinity, protein was serially titrated in ATPase buffer (50 mM MOPS pH 7.4, 5 mM DTT, 5 mM $MgCl_2$, 0.01% Tween-20) and incubated with a constant 2 nM fluorescein-labeled 5'ppp 10bp HP RNA for 15 min at 25°C. Readings were taken in the presence of 500 µM ATP. To obtain K_D values, fluorescence intensity and miliPolarization values from triplicate data sets were plotted as a function of protein concentration. Fluorescence intensity or polarization (Y) were plotted against protein (X) concentration, and the hyperbolic dependence was fit to equation 2 to obtain the binding amplitudes (Bmax) and K_D. C is the intercept representing the fluorescence intensity of the RNA in the absence of protein.

Equation 2: $\mathrm{Y} = \frac{\mathrm{Bmax}*\mathrm{X}}{\mathrm{Kd}+\mathrm{X}} + \mathrm{C}$

5'ppp ds39 RNA competition assay was performed by titrating unlabeled 5'ppp ds39 RNA against 10 nM equimolar RIG-I-bound 5'ppp 10bp HP RNA (FAM). Changes in fluorescence polarization of the 5'ppp 10bp HP RNA (FAM) were monitored (Y) and plotted against 5'ppp ds39 RNA (X) concentration. The inverse hyperbolic dependence was fit to equation 1 to obtain the half maximal inhibitory concentration (IC_{50}). From these experiments, the Cheng-Prusoff equation (equation 3) was used to obtain 5'ppp ds39 RNA K_i values, which are representative of RIG-I's binding affinity for 5'ppp ds39 RNA (K_D).

Equation 3: $K_i = \frac{IC_{50}}{1+\frac{[L]}{K_D}}$

Radiometric ATPase Assay

ATP hydrolysis was measured at variable 5'ppp ds39 RNA and RIG-I concentrations in the presence of 2 mM ATP (spiked with [γ-^{32}P] ATP). The ATPase reaction was measured after 0 (prequench), 20 and 40 minutes of reaction time in ATPase buffer (50 mM MOPS pH 7.4, 5 mM DTT, 5 mM $MgCl_2$, 0.01% Tween-20) at 25°C. Reactions were stopped at each time point using 4 N formic acid and analyzed by PEI-Cellulose-F TLC (Merck) developed in 0.4 M potassium phosphate buffer (pH 3.4). TLC plates were

exposed to a phosphoimager plate, imaged on a Typhoon phosphor-imager, and quantified using the ImageQuant software. The molar [Pi] generated during the reaction time intervals was plotted against time and fit to a linear equation to obtain the ATPase rate (Moles Pi/s). The ATPase-based RNA competition assay was performed by titrating G731R protein against 50 nM WT RIG-I in the presence of 20 nM 5'ppp ds39 RNA. ATPase rates were divided by the 20 nM RNA (Y) and plotted against G731R protein (X) concentration. The inverse hyperbolic dependence was fit to equation 1 to obtain the half maximal inhibitory concentration (IC50). Top represents the Y-intercept in the absence of G731R inhibition, and Bottom represents the baseline of ATPase at maximum inhibition.

NADH-coupled ATPase activity assay

Fluorescence measurements were performed on a Tecan Spark microplate reader in a 384-well black plate at 25°C. The measurements were made with an excitation wavelength of 335 nm, excitation bandwidth of 5 nm, an emission wavelength of 440 nm, and an emission bandwidth of 20 nm. To measure ATPase activity 25 µL reactions consisting of 1X ATPase buffer (50 mM MOPS pH 7.4, 5 mM $MgCl_2$, 5 mM DTT, 0.01% Tween 20) was mixed with an NADH coupled mix (200 µM NADH, 1 mM PEP, 30 U/mL PK, 30 U/mL LDH), 5 nM RIG-I, and 50 nM FAM labelled 5'ppp 10bp HP RNA. Reactions were incubated at 25°C for 15 minutes. Reactions were initiated with 1 mM ATP and fluorescence emission readings were taken every 30 seconds for up to an hour. Fluorescence (Y) was plotted over time in seconds (X) and the resulting linear curve was converted into µM ATP hydrolyzed (Y) over time (X) using a NADH calibration curve. The resulting slope of the linear curve was divided by RIG-I concentration (µM) to obtain the ATPase rates.

To obtain the apparent K_D values for RNA binding using the ATPase activity, 25 µL reactions consisting of 1X ATPase buffer, NADH coupled mix, and 200 nM FAM labelled ds26 Stem RNA were serially titrated with RIG-I (0-2.5 µM). Reactions were allowed to incubate at 25°C for 15 minutes and initiated with 1 mM ATP and time courses were measured. Calculated ATPase rates (Y) were plotted over RIG-I

concentration (X) and the resulting curve was fitted to a hyperbola + intercept equation to obtain the apparent K_D values.

Mant-ATP binding assay

Fluorescence intensity measurements were performed on a Tecan Spark microplate reader in a 384-well black plate at 25 ◦C. A monochromator was set to 290 nm for excitation and 425 nm for emission, with a 20 nm bandwidth. Mant-ATP (Invitrogen Life Technologies) was serially titrated in ATPase buffer (50 mM MOPS pH 7.4, 5 mM DTT, 5 mM $MgCl_2$, 0.01% Tween-20), and baseline fluorescence readings were taken. 500 nM protein was then added to each well containing Mant-ATP and incubated for 15 min at 25ºC before a second fluorescence measurement was taken. The difference in fluorescence intensity readings before and after adding protein was plotted as a function of Mant-ATP concentration. The Δfluorescence intensity (Y) was plotted against Mant-ATP (X) concentration, and the hyperbolic dependence was fit to equation 2 to obtain the binding amplitudes (Bmax) and K_D. C is the intercept representing the fluorescence intensity of the protein alone.

Hydrogen-Deuterium Exchange – Mass Spectroscopy (HDX-MS)

HDX-MS analysis: Ten micromoles of WT RIG-I or G731R mutant in buffer (50 mM HEPES, pH 7.4, 150 mM NaCl, 5% glycerol, 5 mM $MgCl_2$, 2 mM DTT) were optionally incubated with 5'ppp 10bp HP RNA ligand at a 1:1.2 molar ratio (protein: ligand) for 1 h before the HDX reactions at 4 °C. Five microliters of protein with or without RNA was diluted into 20 µL D_2O in exchange buffer (50 mM HEPES, pH 7.4, 150 mM NaCl, 5 mM $MgCl_2$, 2 mM DTT) and incubated for various HDX time points (e.g., 0, 30, 60, 300, 600, 900, 1800, and 3600 s) at 4°C and quenched by mixing with 25 µL of ice-cold 4 M guanidine hydrochloride and 1% trifluoroacetic acid. Dmax samples were incubated in D_2O in the exchange buffer containing 3 M guanidine hydrochloride (50 mM HEPES, pH 7.4, 150 mM NaCl, 5 mM $MgCl_2$, 2 mM DTT, and 3 M guanidine hydrochloride) overnight at room temperature. The sample tubes were immediately placed on dry ice after quenching until the samples were injected into the HDX platform. Upon injection, samples were passed through an immobilized pepsin column (2 mm × 2 cm) at 200 µL/min, and the digested peptides were captured on a 2 mm × 1 cm C8 trap column

(Agilent) and desalted. Peptides were separated across a 2.1 mm × 5 cm C18 column (1.9 μm Hypersil Gold, ThermoFisher) with a linear gradient of 4–40% CH_3CN and 0.3% formic acid, over 5 min. Sample handling, protein digestion, and peptide separation were conducted at 4°C. Mass spectrometric data were acquired using an Orbitrap mass spectrometer (Q Exactive, ThermoFisher) with a measured resolving power of 65,000 at m/z 400.

HDX analyses were performed duplicate or triplicate, with single preparations of each protein ligand complex. The intensity weighted mean m/z centroid value of each peptide envelope was calculated and subsequently converted into a percentage of deuterium incorporation. In the absence of a fully deuterated control, corrections for back exchange were made by an estimated 70% deuterium recovery, and accounting for the known 80% deuterium content of the deuterium exchange buffer. When comparing the two samples, the perturbation %D is determined by calculating the difference between the two samples. HDX Workbench colors each peptide according to the smooth color gradient HDX perturbation key (%D) shown in each indicated figure. Differences in %D between -5 to 5% are considered nonsignificant and are colored gray according to the HDX perturbation key. In addition, unpaired t tests were calculated to detect statistically significant ($p < 0.05$) differences between samples at each time point. At least one time point with a p value <0.05 was present for each peptide in the data set further confirming that the difference was significant.

Peptide identification: Peptides were identified using tandem MS (MS/MS) with an Orbitrap mass spectrometer (Q Exactive, ThermoFisher). Product ion spectra were acquired in data-dependent mode with the top five most abundant ions selected for the production analysis per scan event. The MS/MS data files were submitted to Mascot (Matrix Science) for peptide identification. Peptides included in the HDX analysis peptide set had a MASCOT score >20, and the MS/MS spectra were verified by manual inspection. The MASCOT search was repeated against a decoy (reverse) sequence and ambiguous identifications were ruled out and not included in the HDX peptide set.

Data rendering: The HDX data from all overlapping peptides were consolidated to individual amino acid values using a residue averaging approach. Briefly, for each

residue, the deuterium incorporation values and peptide lengths from all overlapping peptides were assembled. A weighting function was applied in which shorter peptides were weighted more heavily, and longer peptides were weighted less. Each of the weighted deuterium incorporation values was then averaged to produce a single value for each amino acid. The initial two residues of each peptide, as well as prolines, were omitted from the calculations.

Stopped-Flow Off Rate Measurements

RNA off-rates were measured at 25°C using a stopped-flow instrument (Auto-SF 120, Kintek Corp, Austin, Tx). To initiate the reaction, 50 nM 5'ppp ds27 DY547-labelled RNA and 50 nM RIG-I or mutant protein in ATPase buffer (50 mM MOPS pH 7.4, 5 mM DTT, 5 mM $MgCl_2$, 0.01% Tween-20) (pre-incubated at 25°C for 10 min) from syringe A was mixed with a 20-fold excess of an RNA trap (unlabeled 5'ppp ds24 palindromic RNA) from syringe B, with or without 2 mM ATP. The fluorescence emission of DY547 was measured using a 570 nm band-pass filter after excitation at 547 nm. The change in fluorescence intensity was plotted as a function of time, and the data were fit to the sum of two exponentials (equation 4) to estimate the off-rates for each unbinding phase.

Equation 4: $$Y = Plateau + SpanFast \times e^{-KFast \times X} + SpanSlow \times e^{-KSlow \times X}$$

$$SpanFast = 0.01 \times PercentFast \times (Y_o - Plateau)$$

$$SpanSlow = 0.01 \times (-PercentFast + 100) \times (Y_o - Plateau)$$

QUANTIFICATION AND STATISTICAL ANALYSIS

All the experiments were performed as duplicates or triplicates or independent experiments as indicated in the figure legends. Statistical analysis of the difference in data was performed using an unpaired parametric t test design or one-sample t-test in Prism GraphPad. Annotations for statistical differences are indicated in the figures as follows: ns → no significant difference, (*) → $p < 0.05$, (**) → $p < 0.01$, (***) → $p < 0.001$, (****) → $p < 0.0001$.

REFERENCES

FIGURE LEGENDS

Figure 1. Novel RIG-I G731R mutation identified in a severe COVID-19 patient.

(A) Domain structure of human RIG-I. The arrow indicates the G731 location.

(B) RNA- and ATP-induced conformational activation of RIG-I. Top view of apo duck RIG-I (PDB: 4A2W) with CARDs (pink/purple) sequestered to Hel2i domain (green) autoinhibitory interface and helicase domains in an open conformation, semi-closed RNA-bound human RIG-I (PDB: 5F9H), and closed RNA-bound duck RIG-I with ADP·AlF_3 (PDB: 4A36).

(C) Cartoons show the RNA-binding pathway of RIG-I proposed from previous studies[17].

(D) Clustal Omega Multiple Sequence Alignment[53] of helicase motif VI in RIG-I of various species, RLRs, and other SF2 RNA helicases.

(D) Zoomed-in view of motif VI (in pink) in the closed state of RIG-I (PDB: 4A36).

(E) Chromatograms from Sanger sequencing of genomic DNA showing a heterozygous C to G mutation in the patient, indicated by the arrow.

Figure 2. Impaired type I IFN responses in the patient cells upon stimulation with RIG-I specific ligands.

(A) Sanger dideoxy sequencing chromatograms of cDNA from the patient's T cells and monocyte-derived dendritic cells (MoDCs) showing a heterozygous G-to-C transversion corresponding to G731R, indicated by the arrows. HC: healthy control; Pt: patient.

(B) Immunoblot analysis of RIG-I proteins in whole cell lysates (90 μg/lane) from healthy controls (HC, n=4) and patient's cycling T cells, without or with IFN-α stimulation. HSP90 was used as a loading control.

(C-F) Primary monocytes (C), MoDCs (D), or T cells (E, F) from the patient were stimulated for 3 h with the indicated amounts per million cells of intracellular 5'ppp39dsRNA (C, D, and E) or 3p-hpRNA (F). *IFNB1 e*xpression was quantified by

qRT-PCR, normalized to that of *ACTB*, and shown relative to the average of normal controls. Data are mean ± SD from different individuals in each group. Data for unstimulated cells shown in panels (E) and (F) were shared in simultaneously run experiments.

(G) IFN-β promoter response from transfection of RIG-I plasmids (50 ng) into HEK293T RIG-I$^{-/-}$ cells measured by dual luciferase reporter assay (independent RNA transfections, n=3).

(H) hPIV-induced IFNβ reporter luciferase activities for G731R. HEK293T cells were transfected with WT, G731R, or EV along with the IFNβ-Luc and a constitutively expressed Renilla reporter for 6 hours. Cells were then infected with hPIV (MOI 3) for an additional 20 hours before measuring luciferase activity. IFNβ-Luc reporter activity in each condition was normalized to Renilla and then presented relative to WT RIG-I. Data show means ± SD from 3 independent experiments. Statistical analysis was performed using one-sample t-test. ****, P<0.0001.

Figure 3. RIG-I G731R is a loss-of-function variant with a dominant negative phenotype.

(A) Experimental workflow for generating fibroblasts co-expressing WT and G731R RIG-I. Human primary fibroblasts were transfected with Cas9 protein/RIG-I gRNA (RNP) to knock out (KO) RIG-I. KO fibroblasts were then transduced sequentially with lentiviruses expressing WT RIG-I followed by either G731R or empty vector (EV). As an additional control, RIG-I KO cells were also transduced with lentivirus expressing G731R alone. See also Figure S2.

(B) Human primary RIG-I KO fibroblasts, either alone or transduced with RIG-I G731R or WT plus EV (WT+EV), were infected with GFP-expressing hPIV (MOI 0.2) for 24 to 48 h. Representative flow cytometry plots of hPIV-infected cells.

(C) hPIV infection was quantified by the area under the curve (AUC) of GFP MFI and shown relative to that of KO cells in each experiment from 3 independent experiments.

In each experiment, 2 cell lines for G731R and 3 cell lines for WT+EV transduced cells were used.

(D) Human primary RIG-I KO fibroblasts transduced with WT RIG-I, plus either G731R RIG-I (WT+G731R) or EV (WT+EV), were infected with hPIV (MOI 0.2) for 24 to 48 h. hPIV infection was quantified by GFP expression. Shown are flow cytometry plots for a representative experiment.

(E) GFP was quantified by AUC of GFP MFI and shown relative to that of WT+EV cells in each experiment (N=4) (E). Data for WT+EV shown in panels (**C**) and (**E**) were shared in simultaneously run experiments. Statistical analyses were performed using one-sample t-test (F, H). ****, $P < 0.0001$; **, $P < 0.01$.

(F) IFN-β promoter response measured by dual luciferase reporter assay in HEK293T RIG-I$^{-/-}$ cells transfected with a constant amount of WT RIG-I plasmid and 5 nM 5'ppp ds39 RNA, while titrating G731R plasmid. Total plasmid concentration was kept constant by substitution with an empty vector. The error bars represent the standard error of the mean (independent RNA transfection, n=3), and the curve shows the fit of the mean data to equation 1 to obtain the half-maximal inhibitory concentration (IC_{50}).

(G) hPIV-induced IFNβ reporter luciferase activities in cells co-transfected with WT (5 ng) and increasing doses (5 to 20 ng) of G731R or EV plasmids. IFNβ-Luc reporter activity in each condition was first normalized to Renilla and then shown relative to EV. Data show means ± SD from 3 independent experiments. Statistical analysis was performed using one-sample t-test. ***, $P<0.001$

(H) Cells were co-transfected with WT RIG-I (5 ng) and an equal amount (5 ng) of WT RIG-I, G731R RIG-I, or empty vector (EV) plasmids to mimic the indicated genotypes, and then infected with hPIV. IFNβ-driven Firefly luciferase reporter activity for each condition was normalized to *Renilla* luciferase and shown relative to that of the WT/WT condition. RLU, relative light units. Data show means ± SD from 3 independent experiments. Statistical analysis was performed using one-way Anova with Turkey's multiple comparisons test. ****, $P < 0.0001$

Figure 4. RIG-I G731R competitively binds 5'ppp dsRNA in an ATPase deficient manner.

(A) Electrophoretic mobility shift assay of fluorescently labeled 5'ppp ds39 RNA upon addition of WT and G731R RIG-I (representative image from n=3).

(B) 5'ppp ds39 RNA binding affinity (K_D) was obtained using a competitive fluorescence-based RNA binding assay. See Figure S3. First, 5'ppp 10bp HP RNA (FAM) binding affinity (K_D) was measured by changes in fluorescence polarization while titrating RIG-I against constant 2 nM RNA. Next, RIG-I displacement from the 5'ppp 10bp HP RNA (FAM) was monitored by changes in fluorescence polarization while titrating unlabeled 5'ppp ds39 RNA against 10 nM equimolar RIG-I-bound 5'ppp 10bp HP RNA (FAM). The Cheng-Prusoff equation was used to obtain 5'ppp ds39 RNA K_i values, which are representative of RIG-I's binding affinity for 5'ppp ds39 RNA (K_D). Data show means ± SD from 3 independent experiments. Statistical analysis was performed using unpaired t-test. *, $P<0.05$.

(C) ATPase activity of 1 μM WT and G731R RIG-I was measured on 5 nM 5'ppp ds39 RNA using a radiometric ATPase assay (biological replicates, n=3).

(D) Mant-ATP binding to WT and G731R RIG-I using fluorescence-based titration. The differences in the fluorescence intensity of Mant-ATP (F_M) and Mant-ATP with protein (F_{MP}) are plotted against Mant-ATP concentration. The error bars represent the standard error of the mean (n=3), and the curve shows the hyperbolic fit of the mean data to **equation 2** to obtain the Mant-ATP K_D values.

(E) ATPase activity of WT RIG-I with 5'ppp ds39 RNA was measured while titrating in increasing G731R protein. The error bars represent the standard error of the mean (n=3), and the curve represents fitting of the mean data to **equation 1** to obtain the IC_{50} value.

Figure 5. HDX-MS analysis of G731R reveals CARDs-CHL protection.

(A) Linear mapping of the HDX differential data of WT and G731R with and without 5'ppp HP RNA.

(B) The differential HDX pattern of G731R apo vs WT RIG-I apo mapped onto a 3D composite model of G731R apo (4A2W, 3TBK, 4AY2, & computationally modeled CARDs-Helicase Linker, (CHL).

(C) The differential HDX pattern of WT RIG-I ± 5'ppp 10bp HP RNA mapped onto a 3D composite model of RNA-bound WT RIG-I with CARDs exposed (PDB: 5E3H, 4P4H, 4AY2, & computationally modeled CHL. (i) Deuterium uptake plots of select RIG-I peptides represented as percent deuterium uptake over time.

(D) The differential HDX pattern of G731R ± 5'ppp 10bp HP RNA mapped onto a composite model of RNA-bound G731R with CARDs sequestered (PDB: 4A2W, 3TBK, 4AY2, & computationally modeled CHL. (i) Deuterium uptake plots of select RIG-I peptides represented as percent deuterium uptake over time.

Figure 6. The role of CHL in G731R loss of function mechanism

(A) Amino acid sequence of the intrinsically disordered CHL of RIG-I. Negatively charged residues are colored red and underlined; positively charged residues are colored blue. The 190-200 segment is indicated.

(B) IFN-β promoter response of the 10 aa deletion in the CHL (Δ190-200) in WT and G731R RIG-I was measured by the dual luciferase reporter assay in the absence and presence of 5 nM 5'ppp ds39 RNA (independent RNA transfections, n=3). The fold-change between WT and Δ190-200 deletion is shown.

(C) ATPase activity of 1 μM protein on 5 nM 5'ppp ds39 RNA was measured using the radiometric ATPase assay performed three times (biological replicates, n=3). Mean rates of hydrolysis (Moles P_i / Moles RNA / sec) are reported, and the individual data points are plotted over bars representing the mean values with error bars representing the standard error of the mean (SEM).

Figure 7. G731R is trapped in a kinetically unstable CTD-mode

(A) RIG-I forms kinetically distinguishable CTD-mode and Helicase-mode conformations on 5'ppp RNA. Experimental setup to measure the off-rate of RIG-I from 5'ppp RNA in a stopped-flow instrument.

(B) Biphasic kinetics of WT RIG-I and G731R dissociation from 5'ppp ds27 RNA with and without ATP. The time axis is shown on a log scale to clearly show the two phases. The dissociation kinetics (biological replicates, n=3) best fit to the sum of two exponentials (**equation 4**), providing slow and fast off-rates and the corresponding amplitudes.

(C) The fast (CTD-mode) and slow (Helicase-mode) phase amplitudes from data in panel C in the absence of ATP are shown as percent population and their lifetimes (1/off-rate). Three biological replicates are shown with SEM.

(D) The population and lifetimes of CTD-mode and Helicase-mode phases are shown in the presence of ATP. Three biological replicates are shown with SEM.

Figure 8. The G731 mutation leads to both loss and gain of function.

(A) IFN-β response of various G731X mutants with and without RNA was measured by dual luciferase reporter assay (independent RNA transfections, n=3).

(B) PyMOL Mutagenesis Wizard analysis of various G731X mutations in the closed state of RIG-I (4A36). The visible disks indicate pairwise overlap of atomic van der Waals radii.

(C) ATPase activity of 50 nM WT and G731A was measured with and without 5 nM 5'ppp 10bp HP RNA (biological replicates, n=3).

(D) 5'ppp 10bp HP RNA binding affinity (K_D) of WT and G731A was obtained using fluorescence polarization titrations of RIG-I against constant 2 nM RNA (biological replicates, n=3).

(E) ds26 Stem RNA binding affinities of WT and G731A were obtained by measuring ATPase activity at various RIG-I concentrations against a constant 200 nM ds26 Stem RNA. The K_D values obtained from the binding curves are plotted. Note that only two

points are shown for WT as a K_D could not be obtained from one of the curves (biological replicates, n=2). Three points are shown for G731A (biological replicates, n=3).

Figure 9. Model of dominant-negative loss of function activity of G731R RIG-I

Mechanistic model of G731R mutation trapping RIG-I in the CTD-mode RNA-bound conformation, preventing CARDs-CHL exposure, and competitively interfering with wild-type activity.

1 Yoneyama, M. *et al.* The RNA helicase RIG-I has an essential function in double-stranded RNA-induced innate antiviral responses. *Nat Immunol* **5**, 730-737 (2004). https://doi.org/10.1038/ni1087

2 Yoneyama, M. *et al.* Shared and unique functions of the DExD/H-box helicases RIG-I, MDA5, and LGP2 in antiviral innate immunity. *J Immunol* **175**, 2851-2858 (2005). https://doi.org/10.4049/jimmunol.175.5.2851

3 Onomoto, K., Onoguchi, K. & Yoneyama, M. Regulation of RIG-I-like receptor-mediated signaling: interaction between host and viral factors. *Cell Mol Immunol* **18**, 539-555 (2021). https://doi.org/10.1038/s41423-020-00602-7

4 Thoresen, D. *et al.* The molecular mechanism of RIG-I activation and signaling. *Immunol Rev* **304**, 154-168 (2021). https://doi.org/10.1111/imr.13022

5 Rodriguez, K. R., Bruns, A. M. & Horvath, C. M. MDA5 and LGP2: accomplices and antagonists of antiviral signal transduction. *J Virol* **88**, 8194-8200 (2014). https://doi.org/10.1128/JVI.00640-14

6 Solotchi, M. & Patel, S. S. Proofreading mechanisms of the innate immune receptor RIG-I: distinguishing self and viral RNA. *Biochemical Society Transactions* **52**, 1131–1148 (2024). https://doi.org/https://doi.org/10.1042/BST20230724

7 Goubau, D. *et al.* Antiviral immunity via RIG-I-mediated recognition of RNA bearing 5'-diphosphates. *Nature* **514**, 372-375 (2014). https://doi.org/10.1038/nature13590

8 Veit Hornung, J. E., Sarah Kim, Krzysztof Brzózka, Andreas Jung, Hiroki Kato, Hendrik Poeck, Shizuo Akira, Karl-Klaus Conzelmann, Martin Schlee, Stefan Endres, Gunther Hartmann. 5'-Triphosphate RNA is the ligand for RIG-I. *Science* (2006). https://doi.org/10.1126/science.1132505

9 Devarkar, S. C. *et al.* Structural basis for m7G recognition and 2'-O-methyl discrimination in capped RNAs by the innate immune receptor RIG-I. *Proc Natl Acad Sci U S A* **113**, 596-601 (2016). https://doi.org/10.1073/pnas.1515152113

10 Wang, Y. *et al.* Structural and functional insights into 5'-ppp RNA pattern recognition by the innate immune receptor RIG-I. *Nat Struct Mol Biol* **17**, 781-787 (2010). https://doi.org/10.1038/nsmb.1863
11 Fairman-Williams, M. E., Guenther, U. P. & Jankowsky, E. SF1 and SF2 helicases: family matters. *Curr Opin Struct Biol* **20**, 313-324 (2010). https://doi.org/10.1016/j.sbi.2010.03.011
12 Luo, D. *et al.* Structural insights into RNA recognition by RIG-I. *Cell* **147**, 409-422 (2011). https://doi.org/10.1016/j.cell.2011.09.023
13 Jiang, F. *et al.* Structural basis of RNA recognition and activation by innate immune receptor RIG-I. *Nature* **479**, 423-427 (2011). https://doi.org/10.1038/nature10537
14 Kowalinski, E. *et al.* Structural basis for the activation of innate immune pattern-recognition receptor RIG-I by viral RNA. *Cell* **147**, 423-435 (2011). https://doi.org/10.1016/j.cell.2011.09.039
15 Ramanathan, A. *et al.* The autoinhibitory CARD2-Hel2i Interface of RIG-I governs RNA selection. *Nucleic Acids Res* **44**, 896-909 (2016). https://doi.org/10.1093/nar/gkv1299
16 Schweibenz, B. D. *et al.* The intrinsically disordered CARDs-Helicase linker in RIG-I is a molecular gate for RNA proofreading. *EMBO J* **41**, e109782 (2022). https://doi.org/10.15252/embj.2021109782
17 Devarkar, S. C., Schweibenz, B., Wang, C., Marcotrigiano, J. & Patel, S. S. RIG-I Uses an ATPase-Powered Translocation-Throttling Mechanism for Kinetic Proofreading of RNAs and Oligomerization. *Mol Cell* **72**, 355-368 e354 (2018). https://doi.org/10.1016/j.molcel.2018.08.021
18 Wang, W. & Pyle, A. M. The RIG-I receptor adopts two different conformations for distinguishing host from viral RNA ligands. *Mol Cell* **82**, 4131-4144 e4136 (2022). https://doi.org/10.1016/j.molcel.2022.09.029
19 Jang, M. A. *et al.* Mutations in DDX58, which encodes RIG-I, cause atypical Singleton-Merten syndrome. *Am J Hum Genet* **96**, 266-274 (2015). https://doi.org/10.1016/j.ajhg.2014.11.019
20 Lu, C. & MacDougall, M. RIG-I-Like Receptor Signaling in Singleton-Merten Syndrome. *Front Genet* **8**, 118 (2017). https://doi.org/10.3389/fgene.2017.00118
21 Lassig, C. *et al.* Unified mechanisms for self-RNA recognition by RIG-I Singleton-Merten syndrome variants. *Elife* **7** (2018). https://doi.org/10.7554/eLife.38958
22 Kato, H. *et al.* Cell type-specific involvement of RIG-I in antiviral response. *Immunity* **23**, 19-28 (2005). https://doi.org/10.1016/j.immuni.2005.04.010
23 Kato, H. *et al.* Differential roles of MDA5 and RIG-I helicases in the recognition of RNA viruses. *Nature* **441**, 101-105 (2006). https://doi.org/10.1038/nature04734
24 Loo, Y. M. *et al.* Distinct RIG-I and MDA5 signaling by RNA viruses in innate immunity. *J Virol* **82**, 335-345 (2008). https://doi.org/10.1128/JVI.01080-07
25 Kandasamy, M. *et al.* RIG-I Signaling Is Critical for Efficient Polyfunctional T Cell Responses during Influenza Virus Infection. *PLoS Pathog* **12**, e1005754 (2016). https://doi.org/10.1371/journal.ppat.1005754
26 Traut, T. W. Physiological concentrations of purines and pyrimidines. *Mol Cell Biochem* **140**, 1-22 (1994). https://doi.org/10.1007/BF00928361

27 Zheng, J. *et al.* HDX-MS reveals dysregulated checkpoints that compromise discrimination against self RNA during RIG-I mediated autoimmunity. *Nat Commun* **9**, 5366 (2018). https://doi.org/10.1038/s41467-018-07780-z
28 Zheng, J. *et al.* High-resolution HDX-MS reveals distinct mechanisms of RNA recognition and activation by RIG-I and MDA5. *Nucleic Acids Res* **43**, 1216-1230 (2015). https://doi.org/10.1093/nar/gku1329
29 Lei, Y. *et al.* A loosened gating mechanism of RIG-I leads to autoimmune disorders. *Nucleic Acids Res* **50**, 5850-5863 (2022). https://doi.org/10.1093/nar/gkac361
30 Cheng, J. *et al.* Accurate proteome-wide missense variant effect prediction with AlphaMissense. *Science* **381**, eadg7492 (2023). https://doi.org/10.1126/science.adg7492
31 Crow, Y. J. & Casanova, J. L. Human life within a narrow range: The lethal ups and downs of type I interferons. *Sci Immunol* **9**, eadm8185 (2024). https://doi.org/10.1126/sciimmunol.adm8185
32 Su, H. C., Jing, H., Zhang, Y., Members of the, C. H. G. E. & Casanova, J. L. Interfering with Interferons: A Critical Mechanism for Critical COVID-19 Pneumonia. *Annu Rev Immunol* **41**, 561-585 (2023). https://doi.org/10.1146/annurev-immunol-101921-050835
33 Jorgensen, S. E. *et al.* Defective RNA sensing by RIG-I in severe influenza virus infection. *Clin Exp Immunol* **192**, 366-376 (2018). https://doi.org/10.1111/cei.13120
34 Lee, S. *et al.* DDX58 Is Associated With Susceptibility to Severe Influenza Virus Infection in Children and Adolescents. *J Infect Dis* **226**, 2030-2036 (2022). https://doi.org/10.1093/infdis/jiac350
35 Saadat, A. *et al.* Inborn errors of type I interferon immunity in patients with symptomatic acute hepatitis E. *Hepatology* **79**, 1421-1431 (2024). https://doi.org/10.1097/HEP.0000000000000701
36 Roussel, L. *et al.* Human retinoic acid-inducible gene I (RIG-I) deficiency associated with susceptibility to classic Kaposi sarcoma. *J Allergy Clin Immunol* (2026). https://doi.org/10.1016/j.jaci.2026.02.027
37 Sampaio, N. G. *et al.* The RNA sensor MDA5 detects SARS-CoV-2 infection. *Sci Rep* **11**, 13638 (2021). https://doi.org/10.1038/s41598-021-92940-3
38 Najm, R. *et al.* IFIH1 loss of function predisposes to inflammatory and SARS-CoV-2-related infectious diseases. *Scand J Immunol* **100**, e13373 (2024). https://doi.org/10.1111/sji.13373
39 Yin, X. *et al.* MDA5 Governs the Innate Immune Response to SARS-CoV-2 in Lung Epithelial Cells. *Cell Rep* **34**, 108628 (2021). https://doi.org/10.1016/j.celrep.2020.108628
40 Thorne, L. G. *et al.* SARS-CoV-2 sensing by RIG-I and MDA5 links epithelial infection to macrophage inflammation. *EMBO J* **40**, e107826 (2021). https://doi.org/10.15252/embj.2021107826
41 Yamada, T. *et al.* RIG-I triggers a signaling-abortive anti-SARS-CoV-2 defense in human lung cells. *Nat Immunol* **22**, 820-828 (2021). https://doi.org/10.1038/s41590-021-00942-0

42 Yang, D. M., Geng, T. T., Harrison, A. G. & Wang, P. H. Differential roles of RIG-I like receptors in SARS-CoV-2 infection. *Mil Med Res* **8**, 49 (2021). https://doi.org/10.1186/s40779-021-00340-5
43 Chandrasekaran, P. *et al.* Distinct mutations at the same positions of STAT3 cause either loss or gain of function. *J Allergy Clin Immunol* **138**, 1222-1224 e1222 (2016). https://doi.org/10.1016/j.jaci.2016.05.007
44 Bastard, P. *et al.* Autoantibodies against type I IFNs in patients with life-threatening COVID-19. *Science* **370** (2020). https://doi.org/10.1126/science.abd4585
45 Bastard, P. *et al.* Autoantibodies neutralizing type I IFNs are present in ~4% of uninfected individuals over 70 years old and account for ~20% of COVID-19 deaths. *Sci Immunol* **6** (2021). https://doi.org/10.1126/sciimmunol.abl4340
46 Diagnosis and Treatment Protocol for Novel Coronavirus Pneumonia (Trial Version 7). *Chin Med J (Engl)* **133**, 1087-1095 (2020). https://doi.org/10.1097/CM9.0000000000000819
47 Shaw, E. R., Rosen, L. B., Ding, L., Holland, S. M. & Su, H. C. Detection of Neutralizing Anti-Type 1 Interferon Autoantibodies. *Curr Protoc* **2**, e511 (2022). https://doi.org/10.1002/cpz1.511
48 Lamborn, I. T. *et al.* Recurrent rhinovirus infections in a child with inherited MDA5 deficiency. *J Exp Med* **214**, 1949-1972 (2017). https://doi.org/10.1084/jem.20161759
49 Ham, H. *et al.* Germline mutations in a G protein identify signaling cross-talk in T cells. *Science* **385**, eadd8947 (2024). https://doi.org/10.1126/science.add8947
50 Schweibenz, B. D., Solotchi, M., Hanpude, P., Devarkar, S. C. & Patel, S. S. RIG-I recognizes metabolite-capped RNAs as signaling ligands. *Nucleic Acids Res* **51**, 8102-8114 (2023). https://doi.org/10.1093/nar/gkad518
51 Hernandez, N. *et al.* Life-threatening influenza pneumonitis in a child with inherited IRF9 deficiency. *J Exp Med* **215**, 2567-2585 (2018). https://doi.org/10.1084/jem.20180628
52 Yiping Jia, S. S. P. Kinetic Mechanism of GTP Binding and RNA Synthesis during Transcription Initiation by Bacteriophage T7 RNA Polymerase*. *The Journal of Biological Chemistry* **272**, 30147-30153 (1997).
53 Sievers, F. *et al.* Fast, scalable generation of high-quality protein multiple sequence alignments using Clustal Omega. *Mol Syst Biol* **7**, 539 (2011). https://doi.org/10.1038/msb.2011.75

Supplementary Files

This is a list of supplementary files associated with this preprint. Click to download.

- TableS1.xlsx
- Aug102026SupplementalFigures.pdf